THE ASTROPHYSICAL JOURNAL, 454:293–306, 1995 November 20

A MULTIWAVELENGTH STUDY OF 30 DORADUS: THE INTERSTELLAR MEDIUM IN A LOW-METALLICITY GALAXY

A. POGLITSCH, A. KRABBE, S. C. MADDEN,[1] AND T. NIKOLA
Max-Planck-Institut für extraterrestrische Physik, D-85740 Garching, Germany
N. GEIS
Department of Physics, University of California, Berkeley, CA 94720
L. E. B. JOHANSSON
Onsala Space Observatory, S-43992 Onsala, Sweden
G. J. STACEY
Department of Astronomy, Cornell University, Ithaca, NY 14853
AND
A. STERNBERG
Tel Aviv University, Ramat Aviv, Israel 69978
Received 1995 March 3; accepted 1995 June 1

ABSTRACT

We report maps of the 158 μm [C II] fine-structure line, the 63 μm and 146 μm [O I] fine-structure lines, the 2.2 μm H I Brγ line, the 2.1 μm H_2 1–0 $S(1)$ ro-vibrational line, and the 2.6 mm CO (1–0) rotational line toward the 30 Doradus complex in the Large Magellanic Cloud.

Comparing our Brγ map with Hα and Hβ measurements, we find that visual to near-infrared extinction and reddening follow the standard dust extinction law and that the Brγ extinction is small, which allows for a reliable determination of the Lyman-continuum intensity. The Lyman continuum as derived from the Brγ emission and the far-UV derived from the far-infrared continuum match the average spectrum of the exciting stars in the 30 Doradus cluster. The observed H_2 line intensity may be produced in dense clumps exposed to the stellar radiation fields.

The maps of all tracers emphasize a shell-like structure of the 30 Doradus region, which is seen approximately edge-on. The warm molecular gas traced by the H_2 line and the ionized gas traced by the Brγ line are intermixed, while the cold molecular gas as traced by CO (1–0) and the photodissociated gas as traced by [C II] are coextensive over tens of parsecs. This distribution can be explained only by a highly fragmented structure of the interstellar medium that allows UV radiation to penetrate deep into the molecular cloud. Clumpiness is also the key to understanding the extremely high [C II]/CO line intensity ratio. Depending on cloud geometry and physical conditions, the relative beam-filling factors of the partly atomic, partly molecular photodissociated gas as seen in the FIR tracers, and of the purely molecular gas traced by CO, can differ substantially in a clumpy, low-metallicity environment. This effect also leads to a greatly increased H_2/CO conversion factor because a major part of the H_2 molecular gas may be contained in the photodissociation region where CO has been destroyed.

Subject headings: dust, extinction — infrared: ISM: lines and bands — ISM: clouds — ISM: individual (30 Doradus) — ISM: structure — Magellanic Clouds

1. INTRODUCTION

The Magellanic Clouds are the nearest external galaxies, and, therefore, they provide a unique opportunity to study irregular galaxies in much greater detail than other, more distant dwarf galaxies. The Large Magellanic Cloud (LMC), in particular, has all the ingredients that make irregular galaxies such interesting objects: it has a substantially lower metallicity than "normal" galaxies, and its low CO (1–0) brightness seems to indicate a low content of molecular gas. Yet it hosts the most luminous and massive star-forming region in the Local Group: 30 Doradus (Kennicutt 1984). If the LMC truly has a deficiency of molecular gas, then the ratio of star formation rate to molecular gas, or the star-forming efficiency, seems high. If, on the other hand, the low CO luminosity is a result of the decrease in metallicity, then the total H_2 molecular mass could be underestimated by the CO emission. In this case, the star-forming efficiency in irregular galaxies might not be extraordinary relative to normal metallicity galaxies.

The utility of CO as a reliable tracer of molecular mass in low-metallicity molecular clouds is questioned both theoretically and observationally. Theoretical models, however, do not give a unique answer. Depending on the particular assumptions, the effect of low metallicity on the CO-to-H_2 conversion factor, X, can be weak (Dickman, Snell, & Schloerb 1986; Wolfire, Hollenbach, & Tielens 1993) or very substantial (Maloney & Black 1988). Observational evidence for a variable CO-to-H_2 conversion factor comes from estimates of virial masses using CO (1–0) observations. For the LMC, Cohen et al. (1988) and Johansson et al. (1990) find virial masses that are $\sim$6 times higher than the masses derived from the CO luminosity based on the canonical conversion factor, $X = 2.3 \times 10^{20}$ cm^{-2}/K km s^{-1} (Strong et al. 1988).

[1] Present address: NASA Ames Research Center, Moffett Field, CA 94035.

To answer these questions we undertook a multiwavelength study of the 30 Doradus region to obtain more complete information on both the UV radiation field and the physical conditions of the different phases of the ISM, particularly on the photodissociation regions (photon-dominated regions [PDRs]), the transition zones between fully ionized and purely molecular gas. PDRs have been investigated in detail both in Galactic sources and in external galaxies (e.g., Tielens & Hollenbach 1985a, b; Genzel et al. 1985; Haas, Hollenbach, & Erickson 1986, Stutzki et al. 1988; Boreiko, Betz, & Zmuidzinas 1990; Burton, Hollenbach, & Tielens 1990; Stacey et al. 1991a; Howe et al. 1991; Meixner et al. 1992; Madden et al. 1993; Zhou et al. 1993). Previous observations of the 158 μm [C II] line toward single positions in the LMC (Stacey et al. 1991a; Boreiko & Betz 1991) or at multiple positions but low angular resolution (Mochizuki et al. 1994) have indicated that these PDRs could make up a much larger fraction of the ISM than in galaxies with metallicities similar to that of our own Galaxy. This is an effect of the lower metallicity and, consequently, reduced UV extinction by dust which allows the UV light to penetrate deeper into the molecular clouds. Depending on the exact physical conditions, these PDRs could constitute a major repository for molecular hydrogen (Maloney & Black 1988; Poglitsch et al. 1992; Madden et al. 1995). We address the PDR conditions by analyzing maps of the 158 μm [C II], the 63 μm and 146 μm [O I], and the CO ($1 \rightarrow 0$) lines.

From the observer's point of view, 30 Doradus is a very favorable case to study since at a distance of $\sim$50 kpc (Westerlund 1990) it is still close enough to allow a detailed, spatially resolved investigation even in the far-infrared. For example, our beam size of 22″ at 63 μm corresponds to a linear scale of 5.3 pc. Additionally, the visual extinction is low (Caplan & Deharveng 1986) so that measurements at wavelengths longward of 2 μm can be expected to be almost free of extinction, independent of the adopted dust extinction law. Also, the ionizing stellar cluster contained within 30 Doradus has been studied, including the central cluster R136 (cf. Walborn 1991 and references therein; Campbell et al. 1992; De Marchi et al. 1993), which gives a good handle on the UV radiation field. We probe the H II region and the hot, molecular gas with observations of the 2.2 μm H I Brγ and the 2.1 μm H_2 1–0 $S(1)$ lines, respectively.

2. OBSERVATIONS

Observations of the $^2P_{3/2} \rightarrow {}^2P_{1/2}$ [C II] 157.7409 μm line, the $^3P_0 \rightarrow {}^3P_1$ [O I] 145.5255 μm line and the $^3P_1 \rightarrow {}^3P_2$ [O I] 63.1837 μm line were carried out on three flight series with the Kuiper Airborne Observatory (KAO) from Christchurch, New Zealand, in 1991 March and April, in 1992 March and April, and 1993 March. The lines were observed with the MPE/UCB Far-infrared Imaging Fabry-Perot Interferometer (FIFI). Full descriptions of the instrument are given in Poglitsch et al. (1991) and Stacey et al. (1992).

In the long-wavelength setup (for the 146 μm and 158 μm transitions) the spatial response function of each pixel of our 5×5 detector array approximates a circular Gaussian of FWHM 55″ (68″ equivalent disk with a corresponding beam solid angle of 8.3×10^{-8} sr). The geometrical pixel size is 40″ × 40″, referred to the sky. In the short-wavelength setup (63 μm) the beam size is approximately 22″ FWHM with a corresponding beam solid angle of 1.3×10^{-8} sr. The geometrical pixel size is 20″ × 20″. An optical image rotator in the spectrometer compensates for sky rotation. To subtract the thermal background the telescope's secondary mirror was chopped 6′ for the 146 μm [O I] observations and between 6′.5 and 9′ for the [C II] observations, both in the east-west direction at 23 Hz. For the 63 μm [O I] observations the chopper throw was 8′ in the southeast–northwest direction. The telescope was nodded to compensate for differential offsets between object beam and reference beam. Flat-fielding was done with internal hot and cold blackbody loads of known temperatures. For absolute intensity calibration at 158 μm we observed the Orion-KL continuum of 40,000 Jy within our beam (Jaffe et al. 1984). The 146 μm measurements were calibrated using Jupiter which was assumed to emit at the time of the observations like a 132 K blackbody (Hildebrand et al. 1985) of size 42″.7. At 63 μm we calibrated with Jupiter which had a diameter of 42″.2 and a brightness temperature of 128 K (Hildebrand et al. 1985) and with Mars which had a diameter of 8″.6 and an assumed brightness temperature of 220 K (Wright & Odenwald 1980). We estimate the absolute line intensities to be accurate within $\pm$30%.

The [C II] data were taken at 11 different, partly overlapping, partly interleaving array positions, resulting in a 7′ × 7′ mapped area around R136, most of which was fully sampled (one-half beam spacing). The observations required 60 minutes of integration time on the source. Wherever several measurements were available, individual values were weighted by noise and averaged. Absolute positions are accurate to within $\sim$15″. The spectral resolution was 75 km s^{-1} (FWHM). For spectral calibration the H_2S line at 157.7726 μm (Flaud, Camy-Peyret, & Johns 1983) was used. The error in the derived velocity scale is estimated to be $\pm$8 km s^{-1}. For the position centered on R136 (R.A. = $5^h39^m03^s.2$, decl. $-69°07'37''$; [1950]), data were taken by scanning a range of 285 km s^{-1} centered at 250 km s^{-1} v_{LSR}. The two peak positions of [C II] emission are contained within this frame of 5 × 5 pixels. There were no indications of any broad wings in the spectra, and since the contribution from the FIR continuum into the detected bandwidth is also only $\sim$5% of the line intensity, all other positions were observed by fixing the Fabry-Perot at the center velocity.

Two frames centered at the peak [C II] positions, (+40″, +100″) and (−60″, −20″) from R136, were taken in the 146 μm [O I] line. For wavelength calibration the H_2S line at 145.4049 μm (Flaud et al. 1983) was used. Because the line intensity was expected to be much weaker than for the [C II] line, the continuum could not be neglected, and data were taken by scanning a range of 340 km s^{-1} centered at v_{LSR} = 250 km s^{-1}, with a 70 km s^{-1} resolution (FWHM). The total integration time was 50 minutes.

The 63 μm data were taken toward five different positions around the northeast [C II] peak position (+40″, −100″), with respect to R136. One frame was recorded by scanning a range of 250 km s^{-1} centered at v_{LSR} = 250 km s^{-1}, with a 65 km s^{-1} resolution (FWHM). The continuum contribution within the detected bandwidth was weak enough compared to the line emission to allow for the more efficient fixed-wavelength mode; the complete map was therefore taken in this way. We mapped an area of 3′ × 3′. The central 1′ × 1′ was sampled at 0.7 beam spacing and the rest of the map with full beam spacing. The total integration time was 75 minutes.

The CO ($1 \rightarrow 0$) observations were carried out at the SEST telescope in 1987 February. A rectangular grid (11′ × 14′) with 1′ spacing was covered. The data were taken in the frequency-switching mode using a high-resolution acousto-optical spectrometer with a channel separation of 43 kHz. At 115 GHz

the beamwidth and the main beam efficiency were 45″ and 0.67, respectively. Pointing offsets were ~3″.5 in each coordinate.

The 2.1655 μm H I Brγ line and the 2.1212 μm H_2 1–0 $S(1)$ ro-vibrational line were observed from the 2.2 m ESO-MPIA telescope at La Silla with our imaging NIR-spectrometer FAST on its commissioning run in 1990 January. The instrument is described in detail in Krabbe et al. (1993). The spectrometer employs a 62 × 58 pixel InSb direct read-out array from Santa Barbara Research Corporation (SBRC). The focal plane scale is 0″.8 $pixel^{-1}$. The seeing was 1″. For wavelength calibration of the Fabry-Perot interferometer we used the strong H_2 and Brγ emission of the BN/KL and θ Ori region in Orion. We observed the Brγ line toward 27 positions in an area of approximately 3′ × 3′ around R136. The total integration time on the line was 400 s per position. Three frames were taken in the H_2 line, covering an area of 40″ × 120″ northwest of R136 with the same integration time per position as for Brγ.

The Brγ and H_2 data reduction was carried out with the MIDAS package (release JAN88). Standard procedures were used for the removal of hot and cold pixels and cosmic-ray hits, dark-current subtraction, and flat-fielding. Individual exposures were aligned by requiring their peak positions to coincide. Finally, continuum images constructed from off-line images taken on either side of the line were removed from the on-line frames, yielding pure line images. This subtraction also effectively removed any atmospheric foreground emission. As the atmosphere is sufficiently flat around the Brγ line it was unnecessary to divide the single images by a standard star spectrum.

3. RESULTS

3.1. Brγ

The Brγ map is shown in Figure 1 (Plates 16–17) together with an Hα image of the 30 Dor region (Czyzak & Aller 1977). The Brγ emission forms a shell-like structure around the ionizing stellar cluster with R136 at its center. The excellent spatial correlation between the two recombination lines already indicates that there is no unusual extinction or in-source obscuration which would likely affect the Hα line more than the Brγ line.

The peak integrated line intensity in Brγ is 7×10^{-4} ergs s^{-1} cm^{-2} sr^{-1}, and the total flux from the mapped area is 4×10^{-11} ergs s^{-1} cm^{-1}. At an assumed distance of 50 kpc (Westerlund 1990 and references therein), this corresponds to a luminosity of 3×10^3 $L_\odot$ in the Brγ line.

Assuming case B recombination in a "standard" H II region (densities $n_e = n_H = 10^4$ cm^{-3}; $T_e = 10^4$ K) and for negligible 2.2 μm extinction we can derive the (minimum) production rate of Lyman continuum (Lyc) photons required to ionize the mapped region (see, e.g., Osterbrock 1989):

$$N_{\rm Lyc} = \frac{1}{f} \times \frac{L_{\rm Br\gamma}}{L_\odot} \times 3 \times 10^{47}\ {\rm s}^{-1}\,, \qquad (1)$$

where $L_{\rm Br\gamma}$ is the Brγ line luminosity and $f \leq 1$ is the fraction of Lyc photons that are photoelectrically absorbed. The lower limit on the Lyc photon rate required to produce the observed Brγ luminosity is then estimated to be 1×10^{51} s^{-1} by assuming $f = 1$. This number may be compared with the result of $\sim 4.5 \times 10^{51}$ s^{-1} Lyc photons from a spectroscopic analysis of the stars in the 30 Dor cluster over a region of ~3′ diameter (Walborn 1991). With an average Lyc photon energy 23.5 eV (see § 4.3) the Brγ line intensity, $I_{\rm Br\gamma}$, can be translated into a Lyc intensity, $I_{\rm Lyc}$:

$$I_{\rm Lyc} = \frac{1}{f} \times \frac{I_{\rm Br\gamma}}{3.5 \times 10^{-4}} \times \frac{1}{\Lambda}\,, \qquad (2)$$

where the factor $1/\Lambda$ accounts for limb-brightening. Averaged over a 15″ × 15″ region around the peak position north of R136 we observe a Brγ intensity of 3.5×10^{-4} ergs s^{-1} cm^{-2} sr^{-1} from which we derive a Lyc intensity of ≈1 ergs s^{-1} cm^{-2} sr^{-1}.

3.2. CO (1 → 0)

The map of the integrated CO (1 → 0) line intensity, $\int T_R^* dv$, is shown in Figure 2 (Plate 18) superposed on the Brγ image. Most of the CO emission is concentrated between $v_{\rm LSR} = 240$ km s^{-1} and $v_{\rm LSR} = 260$ km s^{-1}. Taking into account the different angular resolutions, the CO and Brγ maps show similar shell-like structures, with one peak to the northeast and a second to the southwest of R136. These peaks, while being close to the brightest regions in the Brγ map, are consistently offset toward larger radial distances from R136. The CO (1 → 0) line is commonly used as a tracer of (cold) molecular gas in both Galactic and extragalactic sources (see, e.g., Blitz 1987 and references therein; Young & Scoville 1982; Sanders, Scoville, & Solomon 1985; Bloemen 1989 and references therein). The conversion factor, $X = N_{H_2}/I_{CO}$, however, may depend on the detailed physical parameters and on the metallicity of the ISM and is a subject of discussion (Israel 1988; Maloney & Black 1988; Wolfire et al. 1993). Cohen et al. (1988) have done a large-scale CO (1 → 0) survey of the LMC. They find that the CO luminosity, L_{CO}, as a function of velocity spread, Δv, is similar to that found in the Galaxy, yet a factor of about 6 lower. Using the virial argument one can then conclude—given similar physical conditions otherwise—that the H_2/CO conversion factor is therefore 6 times higher than the Galactic value of $X = 2.3 \times 10^{20}$ cm^{-2}/K km s^{-1} (Strong et al. 1988). This translates into a conversion factor $X_{\rm LMC} = 1.4 \times 10^{21}$ cm^{-2}/K km s^{-1} for the LMC. With this conversion factor we derive H_2 column densities $N(H_2) = 1.2 \times 10^{22}$ cm^{-2} toward the northeast peak and $N(H_2) = 0.8 \times 10^{22}$ cm^{-2} toward the southwest peak. The total molecular mass within the mapped area is 9×10^4 $M_\odot$.

3.3. H_2

Our map of the 2.12 μm H_2 line is shown in Figure 3 (Plate 19) overlaid on the Brγ image of the 30 Dor region. The H_2 emission appears highly fragmented. The apparent coexistence of ionized and molecular gas as well as the fragmented morphology suggests a clump or filamentary structure of the interstellar medium. A representative value for the H_2 line intensity from these clumps is $I_{H_2} = 7.5 \times 10^{-18}$ W m^{-2} $arcsec^{-2}$ $= 1.6 \times 10^{-4}$ ergs s^{-1} cm^{-2} sr^{-1}.

Interstellar vibrational H_2 emission can be produced by many processes (Sternberg 1993) including collisional excitation in gas heated dynamically in shock waves (Draine, Roberge, & Dalgarno 1983) or radiatively in PDRs (Sternberg & Dalgarno 1989; Burton, Hollenbach, & Tielens 1990) or in clouds exposed to X-rays (Draine & Woods 1990). H_2 emission may also be produced by nonthermal processes including molecular formation on grain surfaces or by gas-phase reactions (Black, Porter, & Dalgarno 1981; Hollenbach & McKee 1989), collisional excitation by nonthermal electrons (Gredel & Dalgarno 1995), and the molecular absorption of ultraviolet

PLATE 16

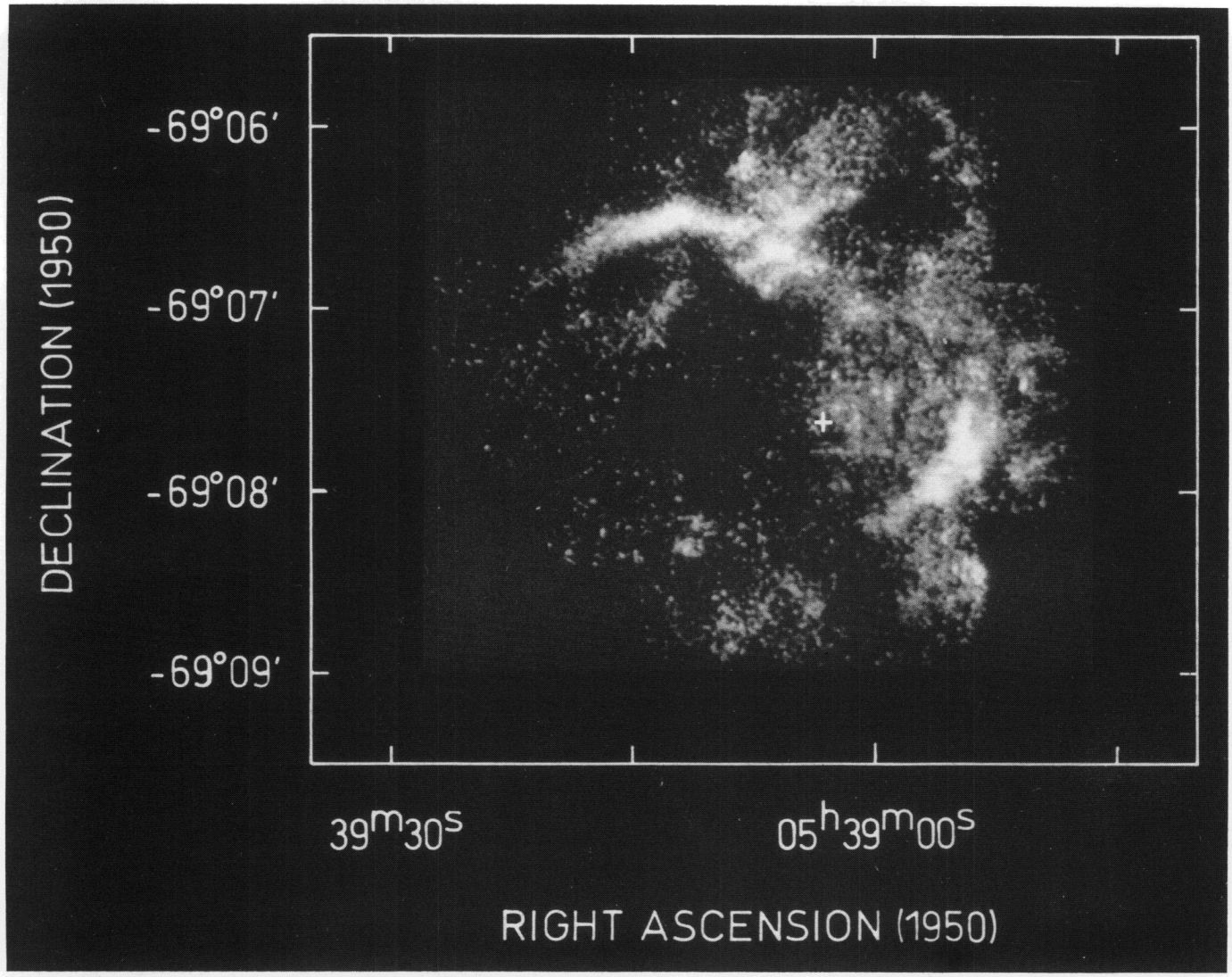

FIG 1*a*

FIG. 1.—The 30 Doradus H II region in the light of hydrogen recombination lines. (*a*) Brγ integrated line intensity image of 30 Doradus; the position of R136 is indicated by the cross. The peak integrated line intensity is 7×10^{-4} ergs s^{-1} cm^{-2} sr^{-1}. (*b*) Hα image of 30 Doradus (Czyzak & Aller 1977).

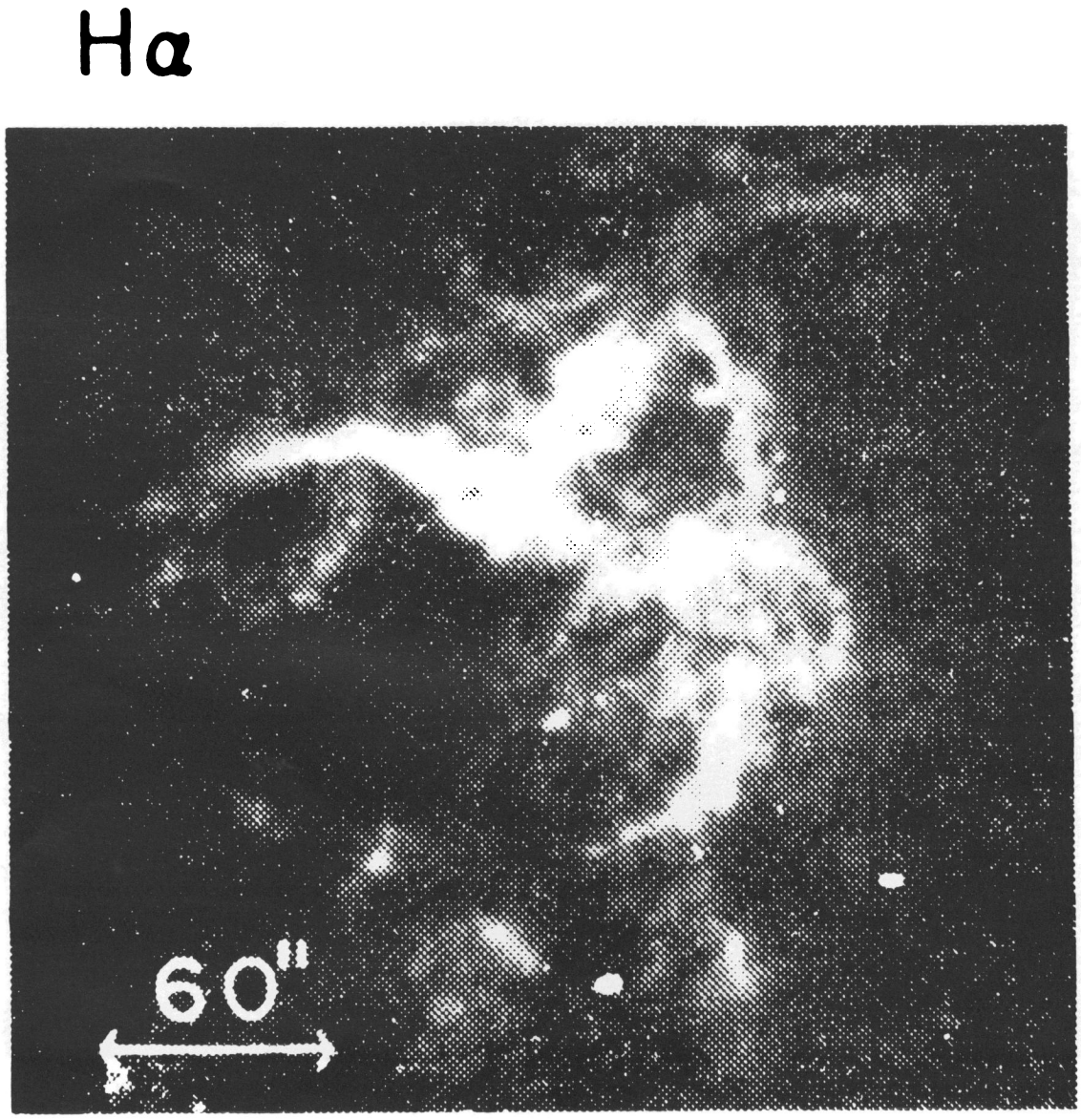

FIG. 1*b*

POGLITSCH et al. (see 454, 295)

PLATE 18

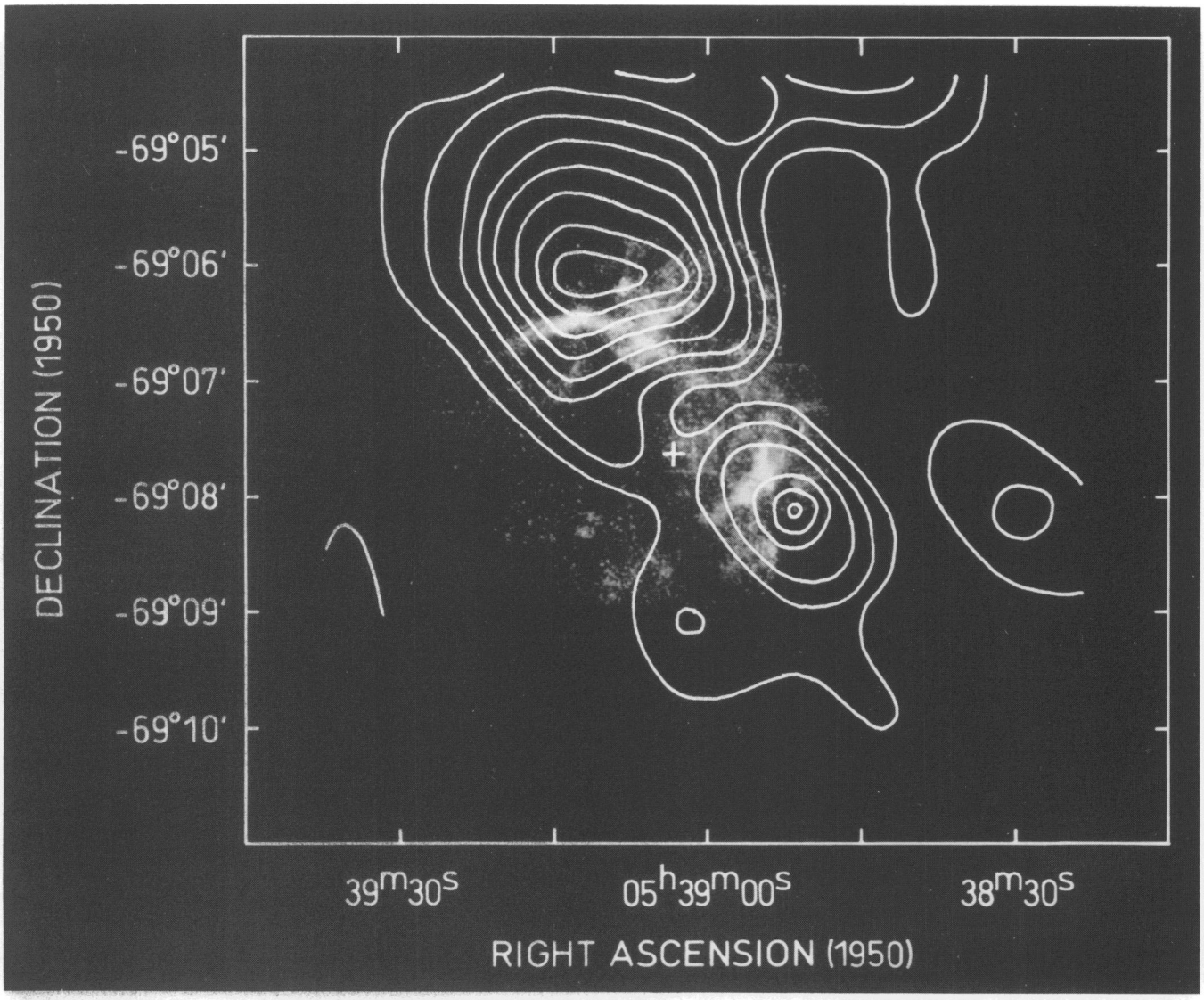

FIG. 2.—Contour map of the CO (1–0) integrated line intensity toward 30 Doradus, superposed on the Brγ image. The contour interval is 1 K km s^{-1}. For conversion to main beam intensity, the map has to be divided by the main beam efficiency (0.67), i.e., the contour interval is 1.5 K km s^{-1}. The cross indicates the position of R136.

POGLITSCH et al. (see 454, 295)

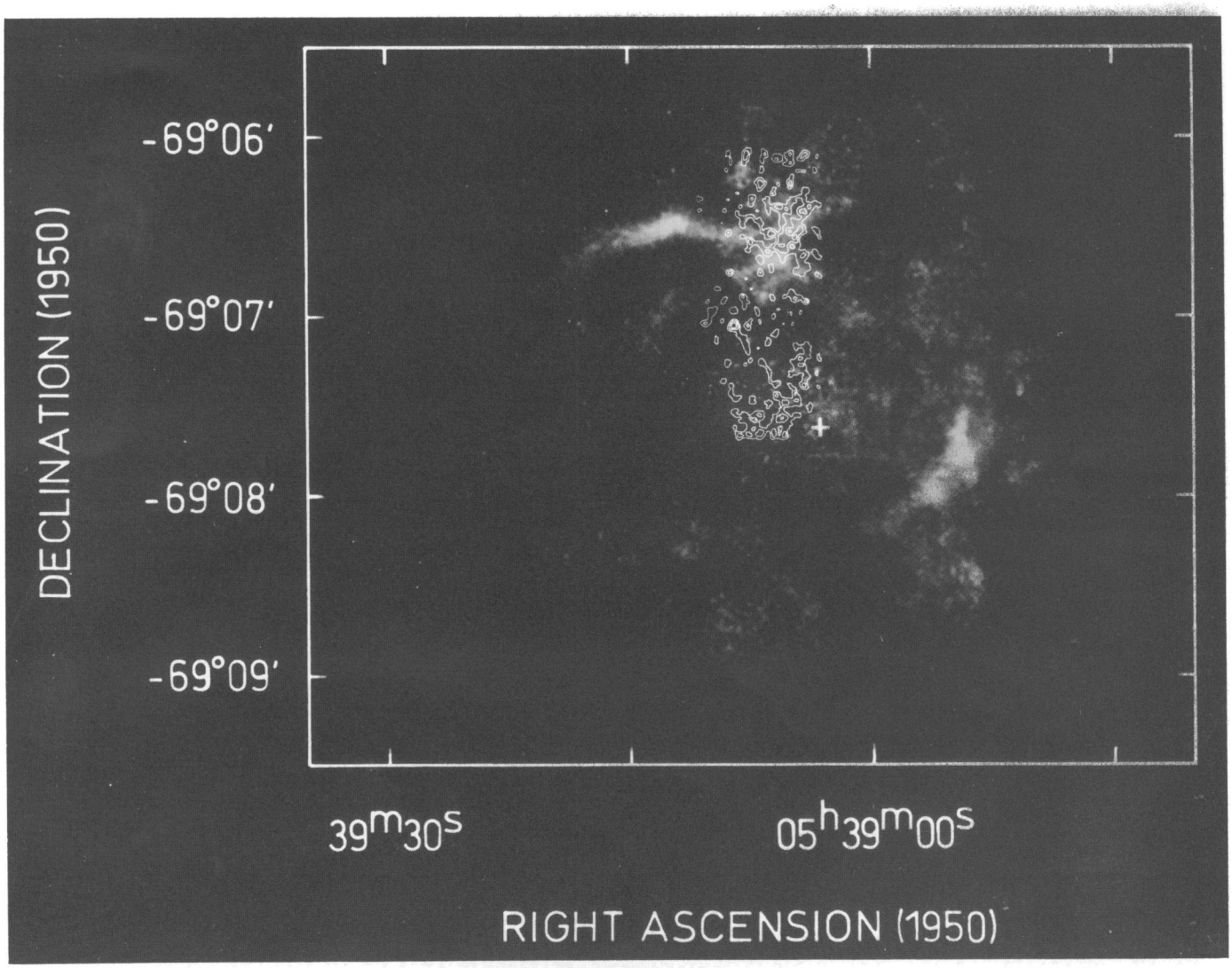

FIG. 3.—Contour map of the H_2 1–0 $S(1)$ integrated line intensity toward 30 Doradus, superposed on the Brγ image. The contour levels are 0.3×10^{-4}, 1.1×10^{-4}, and 2.3×10^{-4} ergs s^{-1} cm^{-2} sr^{-1}. The cross indicates the position of R136.

POGLITSCH et al. (see 454, 295)

photons (Black & van Dishoeck 1987; Sternberg 1988; Goldshmidt & Sternberg 1995).

The origin of the H_2 emission in 30 Dor is uncertain. However, if most of the H_2 emission is collisionally excited in dense, thermally emitting gas, the observed intensity $I_{H_2} = 1.6 \times 10^{-4}$ ergs s^{-1} cm^{-2} sr^{-1} implies hot H_2 column densities of 7×10^{18} cm^{-2} to 5×10^{17} cm^{-2} for temperatures ranging from 1000 K to 2000 K. These values correspond to hot molecular masses of 0.3 $M_\odot$ to 4 $M_\odot$ within our mapped area. Given the total molecular mass of 9×10^4 $M_\odot$ inferred from the CO $(1 \rightarrow 0)$ measurements we find that 3.3×10^{-6} to 4.4×10^{-5} of the H_2 in the 30 Dor region is present in "hot" clouds. Similar fractions of hot molecular gas have been estimated to be present in active galactic nuclei and in the Galactic center (Rotaciuc et al. 1991; Genzel, Hollenbach, & Townes 1994). The FUV field in 30 Dor is $\sim 3500\chi_0$ as inferred from the FIR continuum (Werner et al. 1978). The computations of Sternberg & Dalgarno (1989) show that in hot PDRs exposed to FUV fields $\sim 3 \times 10^3 \chi_0$ the resulting H_2 1–0 $S(1)$ line intensity reaches a limiting value $\sim 1 \times 10^{-4}$ ergs s^{-1} cm^{-2} sr^{-1} for clouds with hydrogen densities equal to about 10^6 cm^{-3}. Thus, much of the observed H_2 emission may be produced in dense $(\sim 10^6$ $cm^{-3})$ molecular clumps exposed to the stellar radiation fields.

3.4. [C II]

The map of the integrated [C II] line intensity is shown in Figure 4 superposed on our CO $(1 \rightarrow 0)$ map. There is a very strong spatial correlation between the two maps: both CO and [C II] peaks are perfectly aligned with each other, and the ratios of the southwest peak to the northeast peak integrated line intensities are almost identical (60% for [C II] and 66% for CO). We find a maximum line intensity of 1×10^{-3} ergs s^{-1} cm^{-2} sr^{-1} toward the northeast peak; the total luminosity of the [C II] line within the mapped area is 6.5×10^4 $L_\odot$ or 0.12% of the total far-infrared luminosity. Both maps also show a protrusion toward the northwest.

The [C II] emission could arise from three components of the ISM: the extended low-density warm ionized medium (ELDWIM), the atomic cold neutral medium (CNM), and the warm PDR layers of dense molecular clouds exposed to strong UV fields. The first two components may dominate the large-scale distribution of [C II] radiation in the Galaxy and other spirals (Heiles 1994; Madden et al. 1993). The third component

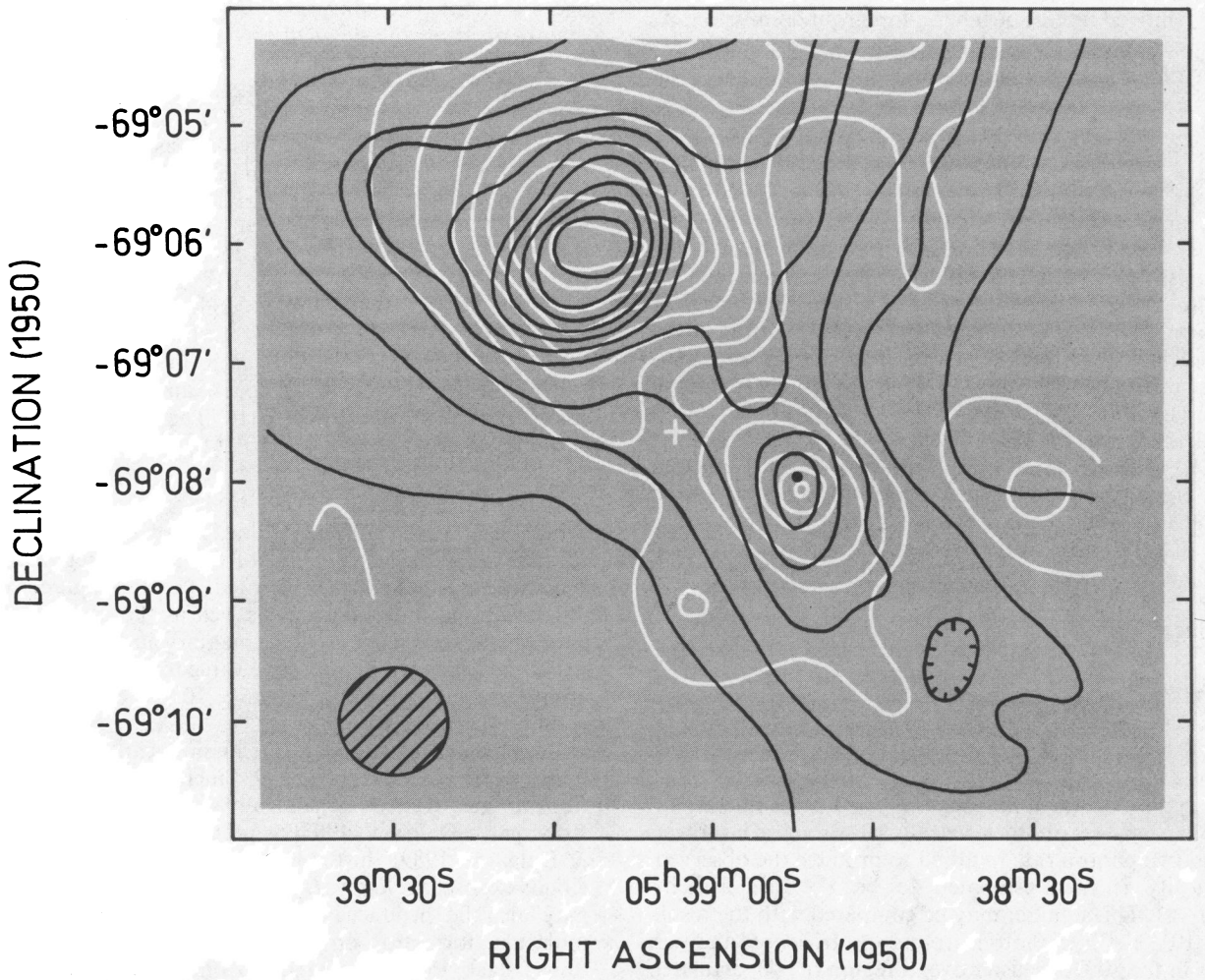

FIG. 4.—Contour map of the [C II] 158 μm integrated line intensity (*black lines*) superposed on the CO (1–0) map (*white lines*). The contour interval is 10^{-4} ergs s^{-1} cm^{-2} sr^{-1}. The hatched circle indicates the [C II] beam size. The cross marks the position of R136.

produces bright [C II] emission but generally has a much smaller filling factor than the diffuse components. The high line intensity and the close correlation with the molecular gas suggest that the [C II] emission observed in 30 Dor arise predominantly from PDRs. The [C II] emission from PDRs can be expected to be optically thin (Stacey et al. 1991b). In this case the integrated line intensity, $I_{[C\,II]}$, is proportional to the hydrogen column density, N_H, contained in the PDR (Crawford et al. 1985):

$$\frac{I_{[C\,II]}}{\text{ergs s}^{-1}\text{ cm}^{-2}\text{ sr}^{-1}} = 7.1 \times 10^{-25} \times \left[\frac{2\exp(-91.3\text{ K}/T)}{1 + 2\exp(-91.3\text{ K}/T) + (n_{crit}/n_H)}\right] \times \frac{X(C^+)}{X_{Gal}(C)}\,\Phi_b\,\frac{N_H}{\text{cm}^{-2}}, \quad (3)$$

where $X(C^+)$ is the gas phase abundance of C^+ relative to hydrogen and $X_{Gal}(C)$ is the Galactic carbon gas phase abundance taken to be 3×10^{-4}, Φ_b is the area filling factor of the source within the beam and n_{crit} is the critical density for collisions with hydrogen. The minimum column density required to explain the observed intensity is obtained in the limit of high temperatures ($T \gg 91.3$ K) and high densities ($n \gg n_{crit}$) for a beam filling factor of 1:

$$\frac{N_H(C^+)}{\text{cm}^{-2}} = 2.1 \times 10^{24}\,\frac{I_{[C\,II]}}{\text{ergs s}^{-1}\text{ cm}^{-2}\text{ sr}^{-1}}\,\frac{X_{Gal}(C)}{X(C^+)}. \quad (4)$$

If we assume that all the gas phase carbon is in the form of C^+ and that the carbon abundance in the LMC is a factor of 3.6 smaller than in the Galaxy (Dufour 1984) we derive a minimum column density of hydrogen nuclei $N_H = 7.5 \times 10^{21}$ cm^{-2}, more than half the column density of the H_2 molecular gas derived above from CO ($1 \rightarrow 0$). Integrated over the mapped area we find a minimum hydrogen mass of $3.7 \times 10^4\ M_\odot$ contained in PDRs. Unless the N_{H_2}/I_{CO} conversion factor that we have used greatly underestimates the amount of hydrogen, we can conclude that the PDR contains most of the interstellar gas. The apparent coexistence of molecular and photodissociated gas over distances $\sim$30 pc suggests a deep penetration of the UV radiation into the molecular cloud, indicating that the ISM must be highly clumped (cf. Stutzki et al. 1988; Meixner et al. 1992).

3.5. [O I] 146 μm

Figure 5 shows the emission spectrum of the [O I] 146 μm line toward the northeast peak in the [C II] and CO ($1 \rightarrow 0$) emission. The total scan width is 250 km s^{-1}, with a spectral resolution of 62 km s^{-1} (FWHM). This is substantially greater than the line width expected from the CO ($1 \rightarrow 0$) observation, and the observed line shape is therefore dominated by the instrumental profile. In order to determine the line intensity and the continuum level, we fitted the observed spectrum with a model line whose shape was obtained by convolving the instrument response with a representative CO line profile plus a (flat) baseline. The result of this fit is also shown in Figure 5. The continuum level agrees well with the results of Werner et al. (1978). The derived integrated intensity in the [O I] line is $8.4 \pm 0.6 \times 10^{-5}$ ergs s^{-1} cm^{-2} sr^{-1}. The quoted error is the statistical uncertainty of the fit and does not include systematic errors, e.g., from the calibration procedure. The intensity drops off too rapidly with distance from the peak to allow mapping.

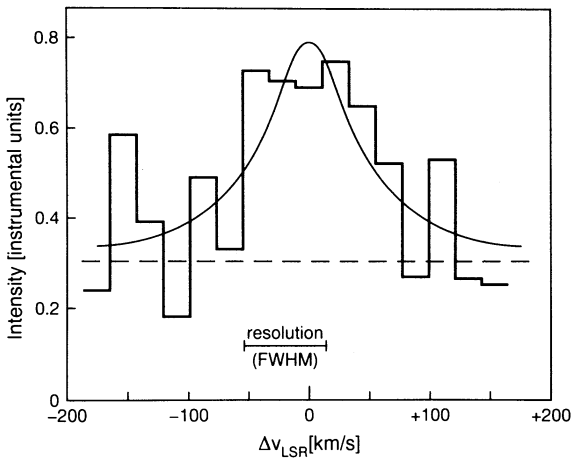

FIG. 5.—Spectrum of the [O I] 146 μm line toward the northeast peak in the [C II] and CO (1–0) emission. The instrumental resolution is 70 km s^{-1} (FWHM). The thin, solid line represents the fitted model spectrum; the broken line shows the continuum level.

3.6. [O I] 63 μm

The map of the [O I] 63 μm integrated line intensity is shown in Figure 6 superposed on the [C II] map. The spatial resolution varies over the map. The beam size in the inner square centered on the northeast [C II] peak is 21″ as defined by the combination of telescope and spectrometer; in the outer parts of the map we convolved the data to a 40″ beam size. This procedure was necessary in order to obtain a uniform noise level over the full map because the effective integration time, including overlap, was about a factor of 6 greater in the central square than for the rest of the map. We find a peak integrated line intensity of $6.1 \pm 0.8 \times 10^{-4}$ ergs s^{-1} cm^{-2} sr^{-1}. The quoted error, again, is the statistical error. The line to continuum ratio at 63 μm can be estimated from the map of Werner et al. (1978). They find a peak flux density of 550 Jy in a 1′ beam, which corresponds to 1.1×10^{-4} ergs s^{-1} cm^{-2} sr^{-1} in our detection bandwidth. Averaged over a 1′ beam we find an integrated line intensity of 4.9×10^{-4} ergs s^{-1} cm^{-2} sr^{-1}. The continuum contamination is therefore $\leq$25% of the line intensity, which is within the systematic error of our calibration. Besides the main peak we find emission extended along the northeast/southwest direction and a tongue of emission toward the northwest that appears to be the beginning of the protrusion seen in the CO ($1 \rightarrow 0$) and [C II] maps.

4. COMPARISON OF DIFFERENT TRACERS AND PHYSICAL PARAMETERS

4.1. *Source Morphology*

The maps of the different tracers emphasize the shell-like structure of the 30 Dor region and an approximately edge-on perspective. The tracers of the ionized gas (Hα, Brγ) peak at the smallest projected radii from the central source R136. The FIR continuum, which traces the FUV at wavelengths longward of the Lyc, peaks at slightly greater radii (Fig. 9). The other tracers that are excited by the FUV ([C II], [O I]), show an interesting peculiarity: the peaks in the [C II] emission and the 63 μm [O I] emission show a small, but significant offset of $\sim$20″ (Fig. 6). While the 63 μm [O I] line is perfectly correlated with the FIR peak, the [C II] emission peaks at a somewhat larger radius, possibly reflecting a gradient in the FUV field and in the gas temperature. The thermal dust emission in the

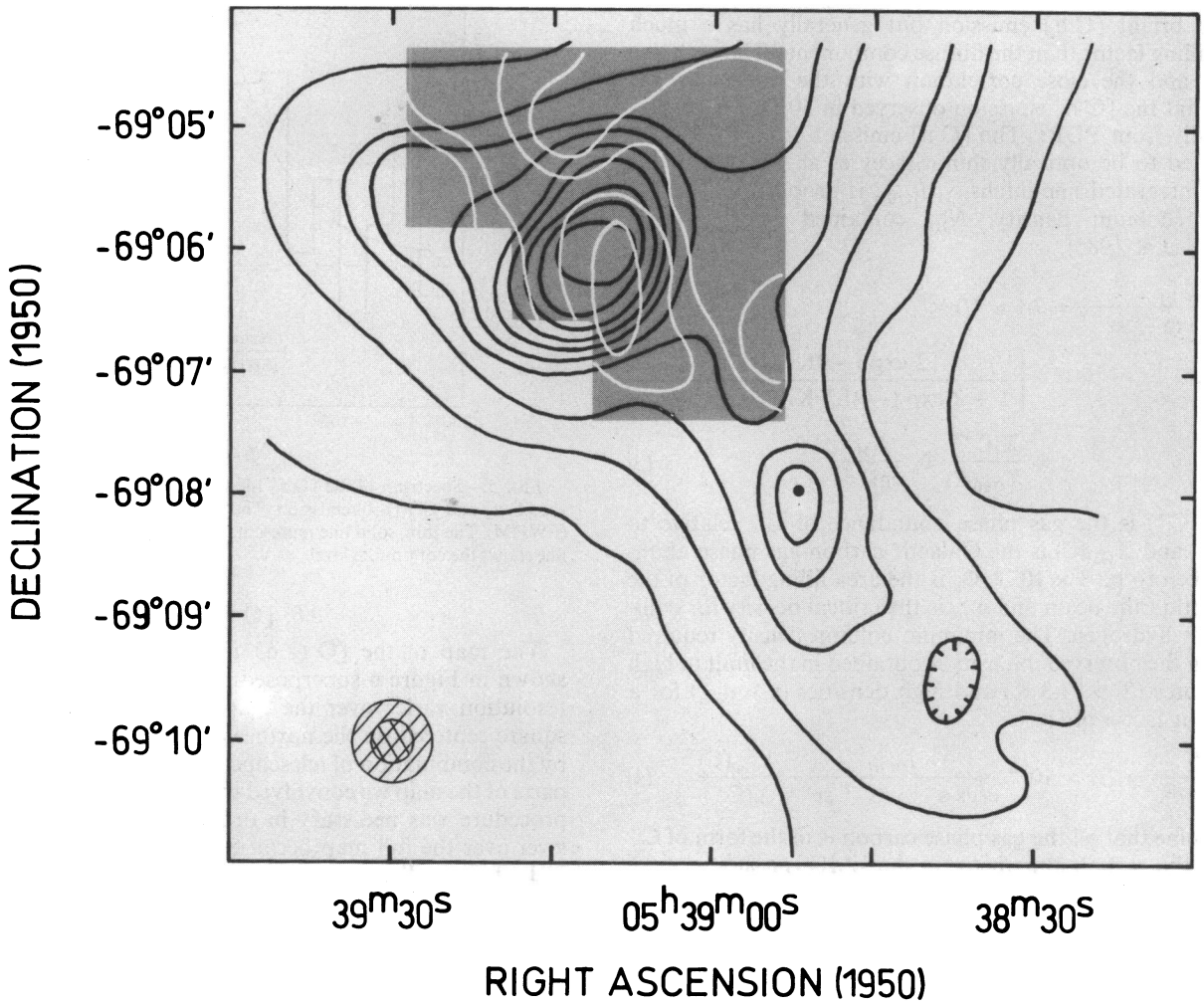

FIG. 6.—Contour map of the [O I] 63 μm integrated line intensity (*white lines*) superposed on the [C II] map (*black lines*). The contour interval is 1.5×10^{-4} ergs s^{-1} cm^{-2} sr^{-1}. The hatched area (*outer circle*) indicates the convolved beam size in the outer parts of the [O I] map: the cross-hatched area (*inner circle*) indicates the beam size in the central square.

FIR is a linear function of the FUV intensity, whereas the [C II] line intensity saturates at higher FUV intensities (Wolfire, Hollenbach, & Tielens 1989). The [C II] peak will therefore represent mainly a peak in column density of photodissociated gas. This conclusion is also supported by the perfect correlation of the [C II] map with the CO ($1 \rightarrow 0$) map, which also traces the column density of molecular gas through the N_{H_2}/I_{CO} conversion. The fact that the molecular and the photodissociated gas appear coextensive over tens of parsecs may be an indicator of a highly clumped state of the ISM, which leads to a much greater apparent UV penetration depth than in a homogeneous medium (Stutzki et al. 1988). The 63 μm [O I] line, on the other hand, requires a greater gas temperature than the [C II] line, and it is expected to be optically thick at typical PDR column densities. High temperatures will therefore enhance the [O I] intensity more than high column densities. This could explain why the [O I] line peaks closer to the source of excitation.

Both the [C II] and the CO emission extend out to substantially greater radii than the tracers of the H II region, indicating the presence of a large amount of gaseous material which is not ionized. On the other hand, the valley between the northeast and the southwest peaks seems to indicate a lack of material rather than a lack of ionization; in fact, this gap could also allow the UV photons to reach the protrusion toward the north seen in all tracers. Czyzak & Aller (1977) came to the conclusion that, at least in first-order approximation, the structure of the 30 Dor H II region is density bounded rather than ionization bounded. Our observations indicate that both situations—ionization bounded (toward the northeast and southwest molecular regions) and density bounded (in the valley)—determine the apparent structure of the H II region.

4.2. Brγ/Hα/Hβ

As becomes apparent from Figure 1, our Brγ and the Hα image by Czyzak & Aller (1977) show qualitatively the same morphology, indicating no substantial in-source obscuration. In a more quantitative approach we compare our Brγ data with the Hα and Hβ photometry results of Caplan & Deharveng (1985) and their analysis in terms of reddening and extinction (Caplan & Deharveng 1986). They performed photometric measurements of the 30 Dor region in the Hα and Hβ lines using a mask of 4'.9 diameter projected on the sky. Figure 7 shows the outline of our Brγ map and the area enclosed by their measurements. They find an Hα line flux of 4.0×10^{-9} ergs s^{-1} cm^{-2} and a ratio Hα/Hβ = 4.57. They derive extinc-

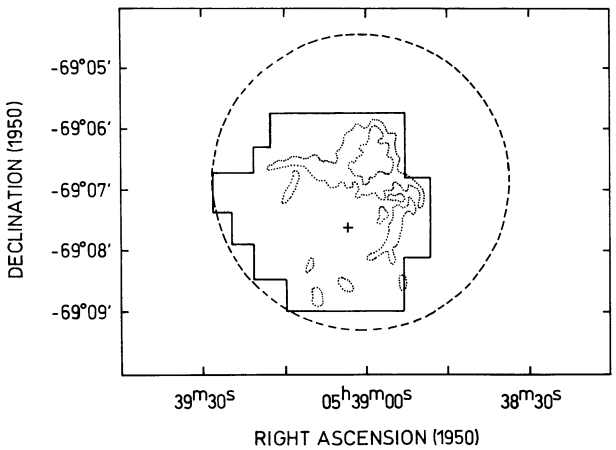

FIG. 7.—Areas covered by photometric measurements in different hydrogen recombination lines. The solid line marks the area mapped in the Brγ line; the dashed line shows the size and position, projected on the sky, of the mask used by Caplan & Deharveng (1985) for the Hα and Hβ measurements. The dotted contours outline the brightest filaments on the Hα image of Czyzak & Aller (1977). The cross indicates the position of R136.

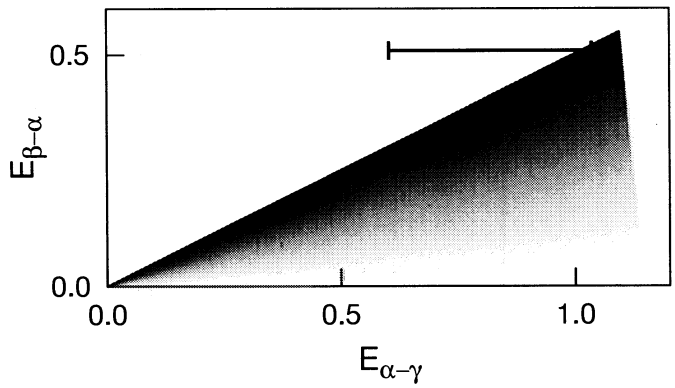

FIG. 8.—Color excess $E_{\beta-\alpha}$ vs. $E_{\alpha-\gamma}$. The solid line represents the ratio that is expected for a homogeneous dust medium "normal" extinction (Savage & Mathis 1979; Draine & Lee 1984). The shaded area indicates the range covered by more complex models with additional free parameters for, e.g., in-source absorption, scattering, or clumped dust. The bar marks the range of values that are compatible with the observations.

tions $A_\beta = 2.1$ and $A_\alpha = 1.6$ by referring their Hα and Hβ intensities to the 6 cm (thermal) radio continuum measured in the same area. These values are higher than expected from the color excess $E_{\beta-\alpha} = A_\beta - A_\alpha = 0.51$ for the case of absorption by a uniform interstellar medium. With the interstellar extinction curve of Savage & Mathis (1979) which also holds for the LMC in the visible and IR (Clayton & Martin 1985; Koornneef 1982; Morgan & Nandy 1982), one derives an Hα extinction $A_\alpha = 1.14$. Caplan & Deharveng discuss the higher extinction they derive in terms of several models such as a clumped ISM or a scattering slab close to the source.

We now want to investigate how our Brγ observations fit into this picture. Of course, the Hα and Hβ measurements only provide quantities averaged over the mask area. In order to derive a color excess $E_{\alpha-\gamma} = A_\alpha - A_\gamma$ it is necessary to estimate the Hα flux from within the area covered by our Brγ map. The size of the Brγ map is 44% of the Hα and Hβ masks. On the other hand, our map includes the brightest filaments, and therefore it is very likely that at least 40% but probably not more than 65% of the observed Hα flux arises from within that area. Within these limits, we derive a color excess $E_{\alpha-\gamma} = A_\alpha - A_\gamma = 0.59$–$1.02$. For comparison with extinction models we show $E_{\beta-\alpha}$ as a function of $E_{\alpha-\gamma}$ in Figure 8. The solid line corresponds to "normal" reddening by a homogeneous dust medium according to the dust model of Draine & Lee (1984) which we used as a representation of extinction measurements in the visible and the near-infrared. The more elaborate models mentioned above all fall in the shaded area below that line. The combination of Hα, Hβ, and Brγ measurements is obviously better represented by the "normal" reddening law. In this case we get a Brγ extinction $A_\gamma \sim 0.1$ corresponding to a correction factor of ~ 1.1 for the Brγ intensity and hence for the derived Lyc luminosity. The question remains then why both the Brγ and the Balmer lines appear too weak compared to the radio continuum (cf. Caplan & Deharveng 1986). A possible reason for the discrepancy could be a nonthermal contribution to the observed radio continuum; there are, indeed, indications of an extended, nonthermal radio source in the core of 30 Dor (Ye, Turtle, & Kennicutt 1991). So, if a significant fraction ($\sim 35\%$) of the presumably thermal 6 cm radio continuum is of nonthermal origin, there is no need to postulate enhanced extinction for the hydrogen recombination lines.

4.3. Brγ/*FIR Continuum*

Interstellar dust is the main absorption medium for the far-ultraviolet continuum (FUV; $h\nu = 6$–13 eV) and visible light emerges from H II regions. The absorbed energy is reradiated in the far-infrared (FIR); in dust enveloped H II regions the FIR continuum is therefore a direct measure for the FUV radiation field (Tielens & Hollenbach 1985a). Lyc radiation is only a minor heating source for the bulk of the dust because of its strong absorption by hydrogen and helium.

The morphology of the 30 Dor region is a nice example of this general picture. In Figure 9 (Plate 20) we compare the Brγ image with the FIR continuum map of Werner et al. (1978). The two peaks in the FIR continuum, tracing the FUV, are closely connected with bright Brγ emission regions which trace the Lyc but which are also slightly radially offset. This is consistent with excitation by the central 30 Dor ionizing cluster.

From the census of the stars comprising the 30 Dor cluster (Walborn 1991) we estimate that we can use the spectral distribution of an O5.5 star as typical for the radiation field. In this case 54% of the total stellar luminosity is emitted as Lyc, with an average photon energy of 23.5 eV, with the rest mainly as FUV radiation (Panagia 1973). From the Brγ intensity averaged over the FIR beam, $I_{\mathrm{Br}\gamma} = 3.5 \times 10^{-4}$ ergs s^{-1} cm^{-2} sr^{-1}, we derive a Lyc intensity $I_{\mathrm{Lyc}} = 1.0$ ergs s^{-1} cm^{-2} sr^{-1}. For an O5.5 spectral distribution the corresponding FUV intensity emerging from the H II region is then 0.85 ergs s^{-1} cm^{-2} sr^{-1} or $4300\chi_0$, where χ_0 is the local Galactic interstellar UV field. The distance from R136 to the main FIR peak, r_{FIR}, is ~ 1.1–$1.2 r_{\mathrm{Br}\gamma}$, where $r_{\mathrm{Br}\gamma}$ is the distance from R136 to the brightest Brγ filament. Thus the FUV flux at the FIR peak, as determined by purely geometrical dilution, corresponds to an equivalent isotropic intensity of $I_{\mathrm{FUV}} = 3100$–$3600\chi_0$. This number agrees with the integrated FIR continuum of Werner et al. (1978), who find $I_{\mathrm{FUV}} = 3500\chi_0$. This further supports the lower value for the Brγ extinction that we derived from Hα, Hβ, and Brγ as compared to the higher value that would follow from the analysis by Caplan & Deharveng (1986).

PLATE 20

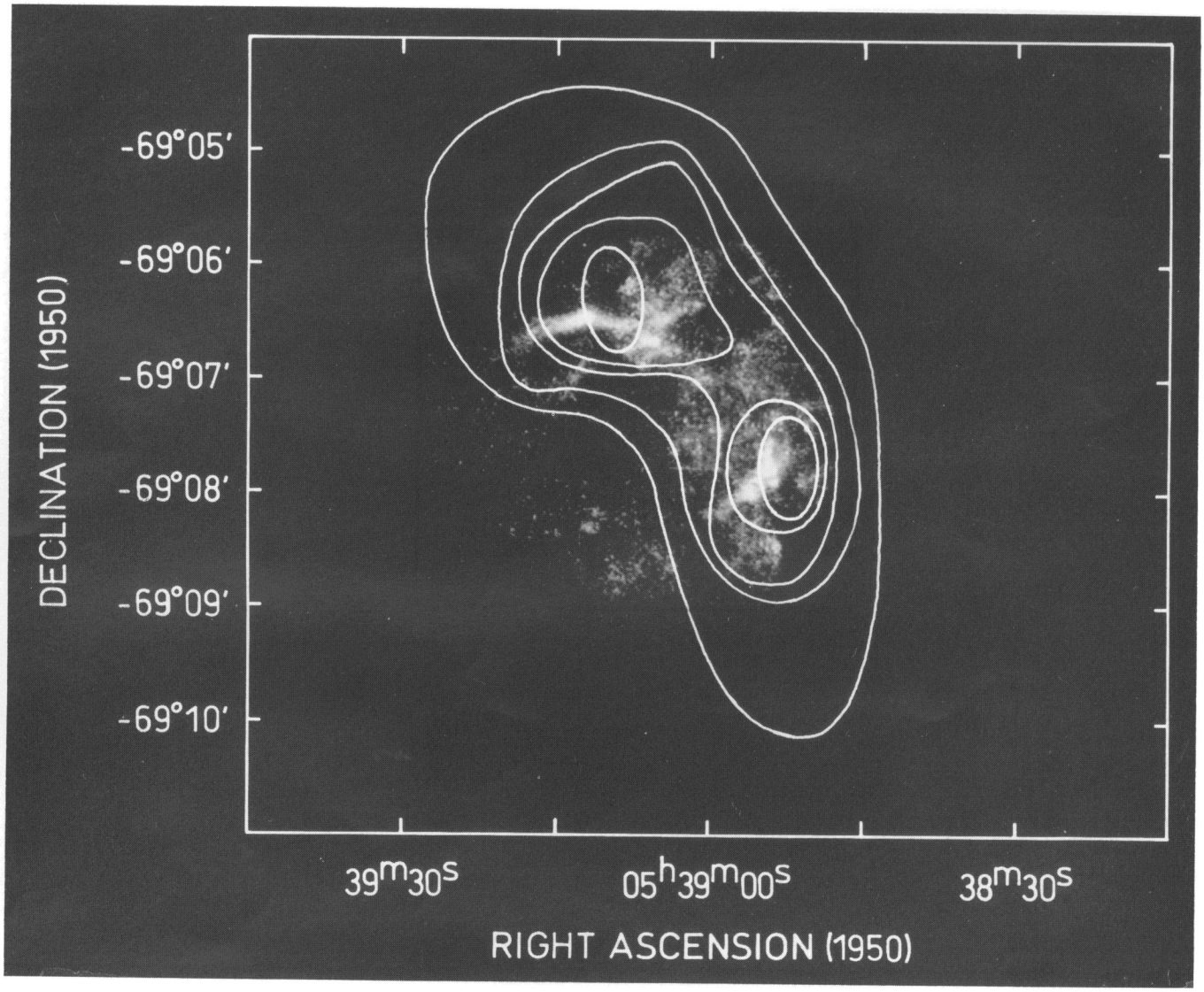

FIG. 9.—Contour map of the integrated FIR continuum (Werner et al. 1978) superposed on the Brγ image of 30 Doradus. The contour interval is 1.44×10^{-1} ergs s^{-1} cm^{-2} sr^{-1}.

POGLITSCH et al. (see 454, 299)

4.4. [C II]/[O I]/CO/*FIR Continuum*

The most complete data set in the FIR tracers is available toward the northeast peak in the [C II] and CO emission; this position will therefore be analyzed in more detail. We will use several approaches to derive the physical parameters and to test the utility of PDR models for a low-metallicity ISM.

4.4.1. *FIR Line Emission from a Single Homogeneous Layer*

Assuming that the [C II] line and both [O I] lines arise from the same component of the ISM, one can use the relative and absolute intensities of these lines to derive a representative temperature, T, hydrogen density, n_H, and column density, N, of the emitting gas. The advantage of this method is that it does not imply any specific model for the heating, cooling, and chemistry in the ISM. The underlying assumption of uniform physical conditions over the emitting region, however, could be a substantial simplification of the real situation. In fact, if the temperature is allowed to vary through the layer, then the three transitions can have very different emitting columns. We used an LVG approximation, escape probability radiative transfer code to simultaneously model the three lines and assumed an abundance ratio of oxygen to carbon of $X_O/X_C = 2$; more details are given in Appendix A.

Figure 10*a*–10*c* show solutions for each observed line intensity ($I_{[C\,II]} = 1 \times 10^{-3}$ ergs s^{-1} cm^{-3} sr^{-1}; $I_{[O\,I]\,146\,\mu m} = 8.45 \times 10^{-5}$ ergs s^{-1} cm^{-2} sr^{-1}; $I_{[O\,I]\,63\,\mu m} = 4.9 \times 10^{-4}$ ergs s^{-1} cm^{-2} sr^{-1}) as a function of n_H and T for three different values of N. The trajectories for the two oxygen lines happen to coincide, within the experimental uncertainty, over a large range of column densities. This is expected if the gas density is less than the critical density of either transition ($n <$ few $\times 10^4$ cm^{-3}) and both lines are optically thin. Therefore, while supporting each other, the [O I] trajectories do not, together with the [C II] trajectory, define a unique solution for n_H, T, and N. We actually find that both the 146 μm [O I] line and the [C II] line are optically thin whereas for the 63 μm [O I] line we find optical depths between 0.5 and 5. Figure 10*d* shows the possible combinations of n_H and T derived from the three line intensities with the C^+ column density, N_{C^+}, as a parameter. It provides a good constraint on the temperature while the density is not well defined.

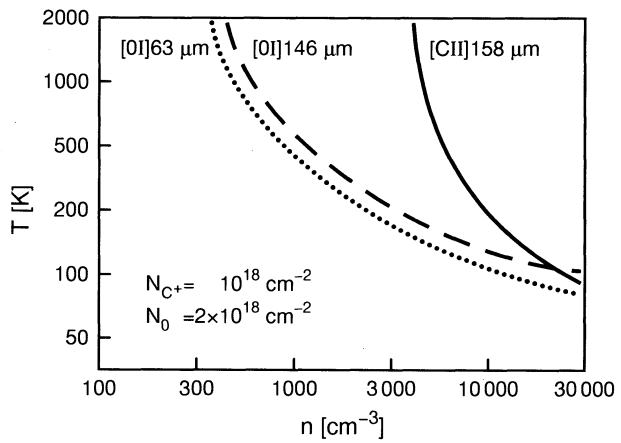

FIG. 10*a*

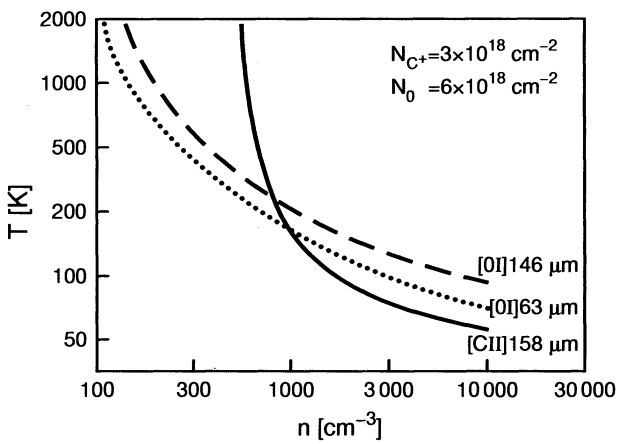

FIG. 10*b*

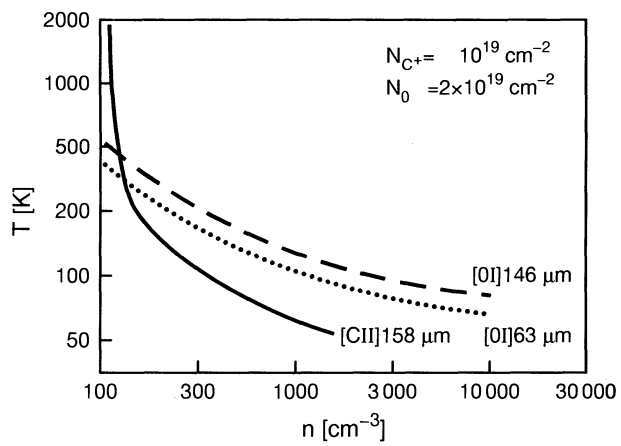

FIG. 10*c*

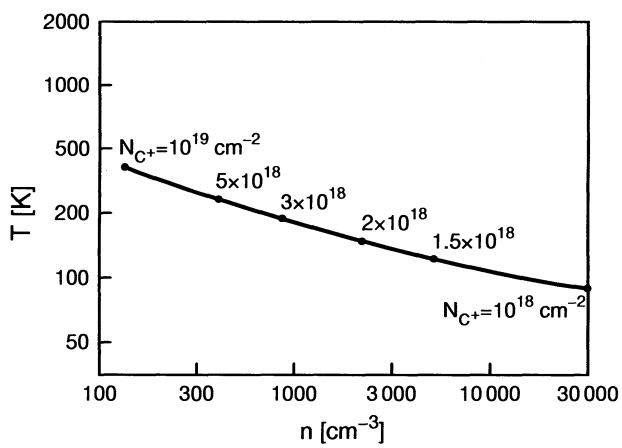

FIG. 10*d*

FIG. 10.—Radiative transver (LVG) calculations for the [C II] 158 μm line, the [O I] 146 μm line, and the [O I] 63 μm line with different column densities of C^+, $N_{C^+} = \frac{1}{2}N_O$. For the respective observed line intensities, combinations of density, n, and temperature, T, have been calculated, with the column density as a free parameter. Three cases are shown: (*a*) $N_{C^+} = 10^{18}$ cm^{-2}; (*b*) $N_{C^+} = 3 \times 10^{18}$ cm^{-2}; and (*c*) $N_{C^+} = 10^{19}$ cm^{-2}. Intersections of the three trajectories define combinations of parameters that match all three observed line intensities simultaneously. Panel (*d*) shows these solutions (n, T) with the column density N_{C^+} as a free parameter.

There are, however, constraints on the maximum C^+ column density. From the integrated CO ($1 \rightarrow 0$) line intensity we derived a molecular hydrogen column density, N_{H_2}, of 1.2×10^{22} cm^{-2} toward the northeast peak, using the conversion factor of Cohen et al. (1988). The most extreme assumption one can make is that all of this gas is contained in the C^+-emitting volume. In this case, with an abundance ratio [C]/[H] $\sim 10^{-4}$, we get $N_{C^+} \sim 3 \times 10^{18}$ cm^{-2} as an upper limit. From Figure 10*d* a lower limit of $n \sim 10^3$ cm^{-3} then follows for the density. On the other hand, Werner et al. (1978) derive a dust temperature $T_{dust} \sim 75$ K. The typical temperature over most of the [C II]–emitting region should then be above 100 K (Tielens & Hollenbach 1985a). This constrains the density to an upper limit of $n \sim 10^4$ cm^{-3}, as seen from Figure 10*d*. We therefore derive a range of temperatures $T = 200$–100 K for densities $n = 10^3$–10^4 cm^{-3}.

4.4.2. *One-dimensional PDR Model*

An alternative way to determine the physical parameters of the PDR is to use detailed models. This method is complementary to the above analysis in that the only free parameters of the model are the density, n, and the UV field, χ. The temperature profile, $T(x)$, and the column density, N, of the PDR are then results of the modeling and not input variables. The advantage of such modeling is a more realistic representation of all physical and chemical parameters as a function of depth into the cloud; the disadvantage is that the model assumes a one-dimensional, face-on geometry. We computed the [C II] and [O I] emission-line intensities using the code and methods described in Sternberg & Dalgarno (1995). In these calculations the thermal balance, molecular chemistry, and FUV radiative transfer are solved self-consistently. In our calculations we have adopted values of 6×10^{-4} and 3×10^{-4} for the total gas phase abundances of oxygen and carbon relative to hydrogen. Our model is expected to be fairly robust with respect to changes in metallicity. Under the assumption that the relative abundances of the interstellar dust and of the heavier elements in the gas phase scale by the same factor, the intensities of the FIR fine-structure lines and the FIR dust continuum have been predicted to depend only weakly on metallicity (Wolfire et al. 1993). Qualitatively this can be understood in the following way: as long as dust extinction is the limiting factor for the FUV penetration into the cloud, the column densities and excitation conditions of the FIR tracers will not be affected much by a change in metallicity; the PDR will just extend over a greater hydrogen column density if the metallicity is decreased.

The results of the model calculation are shown in Figure 11*a* as trajectories in n and χ for a set of line intensities of the 158 μm [C II] line, the 63 μm [O I] line, and the 146 μm [O I] line. The [C II] line has the lowest critical density and level temperature of the three lines; it is therefore thermally populated most easily and does not vary in intensity by more than a factor of 3 over most of the parameter space in Figure 11*a*, whereas the other two lines depend strongly on the density, n, and the UV field, χ. This allows one to determine a solution for n and χ from the three observed line intensities.

Figure 11*b* shows the three trajectories corresponding to the observed line intensities; they apparently do not define a unique solution for n and χ. However, the model calculation was done for a face-on geometry, whereas the 30 Dor region represents much more of an edge-on situation. For the optically thin 158 μm [C II] and 146 μm [O I] lines this could easily lead to a limb-brightening effect, i.e., and enhancement in the observed line intensities due to a larger line-of-sight column density than in the face-on geometry. The optically thick 63 μm [O I] line should not be strongly affected by this effect. In Figure 11*c* a limb-brightening factor of 2 has been assumed for the 158 μm [C II] and 146 μm [O I] lines, i.e., the trajectories shown have been calculated for intensities of half the observed values. The 63 μm [O I] trajectory has been left unchanged. All three trajectories agree well within the experimental uncertainties and provide a good handle on the density n, almost independently of the UV field χ. We find a range in density of $n = 3 \times 10^3$ to 1×10^4 cm^{-3}.

To summarize the results, both methods give similar values for the density, and both temperature and density agree well with the physical parameters found in Galactic PDRs. Similarly, the ratio of the [C II] line intensity to the FIR continuum, $I_{[C\,II]}/I_{FIR} = 1.4 \times 10^{-3}$ toward the northeast peak and $I_{[C\,II]}/I_{FIR} = 0.8 \times 10^{-3}$ toward the southwest peak, is in a range typical for Galactic star formation regions and galactic nuclei (Stacey et al. 1991a).

4.4.3. *Geometry Effect on the* CO ($1 \rightarrow 0$) *Intensity*

On the other hand, the ratios $I_{[C\,II]}/I_{CO} = 6.9 \times 10^4$ toward the northeast peak and $I_{[C\,II]}/I_{CO} = 6.4 \times 10^4$ toward the southwest peak are about an order of magnitude higher than in Galactic star formation regions or the set of external galactic nuclei presented by Stacey et al. (1991a). High $I_{[C\,II]}/I_{CO}$ ratios are also seen in the dwarf irregular galaxy IC 10 (Madden et al. 1995). One-dimensional, semi-infinite, face-on PDR models cannot explain this result: As addressed in the previous section, the [C II] line is expected to depend only weakly on metallicity, and the CO ($1 \rightarrow 0$) emission will always be optically thick and, therefore, not a function of metallicity, either (Wolfire et al. 1993).

As an example we show the model calculation of Stacey et al. (1991a), which follows the method described by Wolfire et al. (1989). In order to determine the physical conditions of PDRs in a situation typical of clumped media or distant sources in which the emitting regions do not entirely fill the beam, they use ratios $Y_{[C\,II]} = I_{[C\,II]}/I_{FIR}$ and $Y_{CO} = I_{CO}/I_{FIR}$. As long as all three species are coextensive, these ratios are independent of beam-filling factors. Figure 12 shows the calculated ratios $Y_{[C\,II]}$ and Y_{CO} for several hydrogen densities, n, and UV fields, χ (Stacey et al. 1991a). The asterisk marks the observed ratios toward the northeast peak in 30 Dor. It falls clearly outside the $Y_{[C\,II]}/Y_{CO}$ combinations covered by the model. The heavy dotted line denotes the expected combination of ratios for the UV field ($\chi = 3600$) and range of densities ($n = 10^3$–10^4 cm^{-3}) derived in the previous sections. It is interesting to note that the observed $Y_{[C\,II]}$ falls well within the predicted range but that the observed Y_{CO} is about an order of magnitude less.

A possible explanation could be that the assumption of equal beam-filling factors is fulfilled for [C II] and the FIR while it does not hold for CO relative to the other two tracers. This situation could exist in an inhomogeneous medium with most of the gas being contained in denser clumps which are embedded in a low-density medium (Goldsmith 1987; Falgarone & Perault 1988; Meixner et al. 1992). Neglecting a possible contribution from the interclump medium, we assume that the FIR continuum and the [C II] and CO ($1 \rightarrow 0$) line emission arise from these clumps as indicated by the fairly high density derived above. Depending on the clump size distribution, the illumination (omnidirectional vs. unilateral), and the

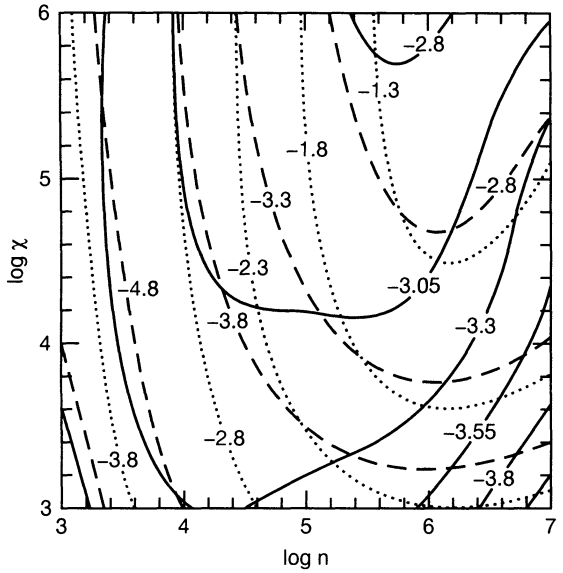

FIG. 11*a*

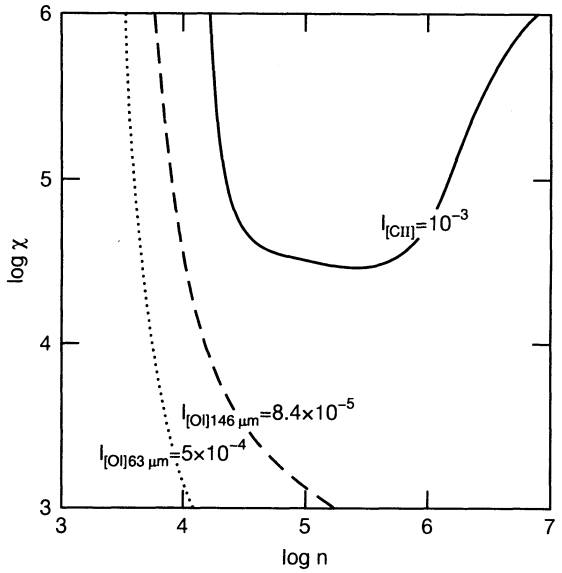

FIG. 11*b*

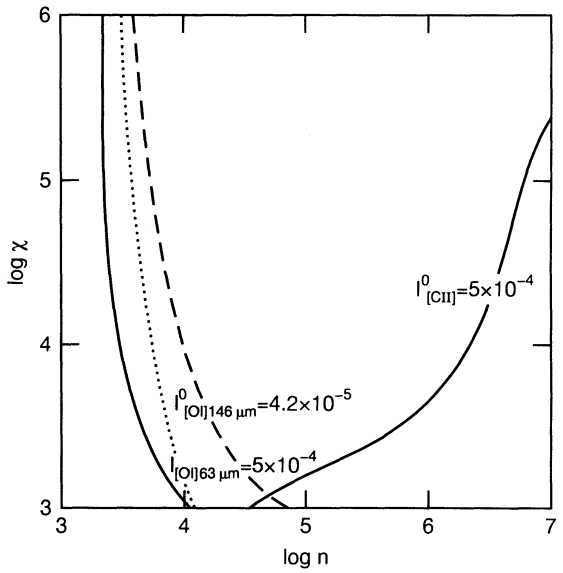

FIG. 11*c*

FIG. 11.—Isointensity contours for the [C II] 158 μm line, the [O I] 146 μm line, and the [O I] 63 μm line as functions of density, n, and UV field, χ, where χ is given in units of the local UV field, $\chi_0 = 2 \times 10^{-4}$ ergs s^{-1} cm^{-2} sr^{-1}. Log intensities are shown as solid lines ([C II], 158 μm), dashed lines ([O I], 146 μm), and dotted lines ([O I], 63 μm). (*a*) For each of the three species, a set of isointensity contours is shown that cover the parameter space typical of Galactic PDRs. Intensities are quoted as logarithm of the integrated line intensity in units of ergs s^{-1} cm^{-2} sr^{-1}. (*b*) Isointensity contours for the observed integrated line intensities toward the northeast peak of 30 Doradus. (*c*) Isointensity contours with integrated line intensities corrected for limb brightening; a limb-brightening factor of 2 has been assumed for the [C II] line and the [O I] 146 μm line.

metallicity, a certain fraction of the volume of a clump will be photodissociated. If we assume optically thin emission in the FIR tracers, i.e., the [C II] line and the dust continuum, then the total emitted power, for a given temperature and density, will be proportional to that volume. We assume that the clumps are substantially smaller than the beam size. For comparison with the one-dimensional, semi-infinite model one can define a relative beam-filling factor Φ_{FIR}/Φ_0 as the ratio of the power emitted from the clump to the power emitted from the semi-infinite medium over a surface area equal to the projected surface area of the clump. For optically thin emission this is equal to the ratio of the emitting volumes.

Similarly, for the CO (1 → 0) line, which for now is assumed to be always optically thick, one can define a relative beam filling factor Φ_{CO}/Φ_0 as the ratio of the projected surface area of the CO-bearing part of the clump to the total projected surface area of the clump. Wolfire et al. (1993) have modeled the CO (1 → 0) emission from a clumpy medium in detail and find only a weak dependence on the metallicity, but they implicitly assume a face-on geometry.

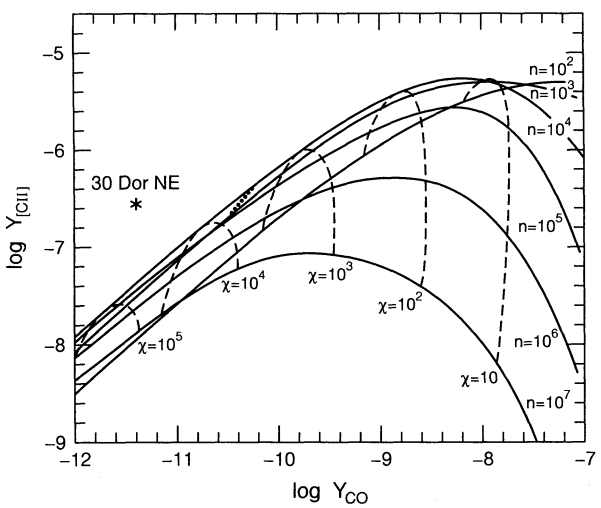

FIG. 12.—Ratios $Y_{[C II]} = I_{[C II]}/I_{FIR}$ vs. $Y_{CO} = I_{CO}/I_{FIR}$. The asterisk marks the observations toward the northeast peak of 30 Doradus. The solid lines represent calculated combinations of $Y_{[C II]}$ and Y_{CO} for a set of constant densities; the dashed lines have been calculated for a set of constant UV fields (after Stacey et al. 1991a). The heavy, dotted line indicates the range of values derived from the FIR continuum and fine-structure line intensities.

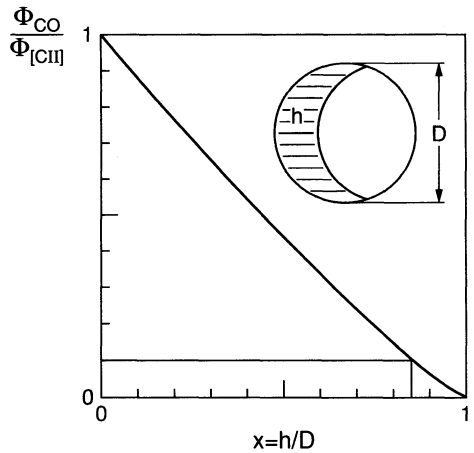

FIG. 13.—Relative beam-filling factors $\Phi_{CO}/\Phi_{[C\,II]}$ for side-illuminated, spherical clumps. The inset shows a cut through a clump. The depth of the photodissociated layer, h, is assumed to be constant over the illuminated part of the clump surface. The graph shows the ratio $\Phi_{CO}/\Phi_{[C\,II]}$ as a function of the normalized depth of the PDR layer, $x = h/D$, where D is the clump diameter.

As a simple model for the 30 Dor region with its shell-like structure and mainly central source of ionization we consider the case of side-illuminated spherical clumps as depicted in Figure 13. We assume that a layer of constant thickness, h, gets photodissociated which is equal in width to the layer in the plane, semi-infinite model. The volume of the remaining core is given by

$$V_{CO} = \tfrac{1}{2}V_0(1 - x)^2(2 + x)\,, \tag{5}$$

where $V_0 = (4/3)\pi R^3$ is the volume of the clump and x is defined as $x = h/D$ with $D = 2R$ being the diameter of the clump. The volume of the FIR-emitting part is then $V_{FIR} = V_0 - V_{CO}$. The relative beam-filling factor is then given by

$$\frac{\Phi_{FIR}}{\Phi_0} = \frac{V_{FIR}}{A_0 h} = \frac{V_{FIR}}{V_0}\frac{2}{3x}\,, \tag{6}$$

where $A_0 = \pi R^2$ is the projected surface area of the clump and $A_0 h$ is the equivalent emitting volume in the plane, semi-infinite geometry. The relative beam-filling factor for the CO emission as defined above is found to be

$$\frac{\Phi_{CO}}{\Phi_0} \equiv \frac{A_{CO}}{A_0} = \frac{2}{\pi}(\arcsin\sqrt{1 - x^2} - x\sqrt{1 - x^2})\,. \tag{7}$$

For comparison with the PDR model (Fig. 12) we then need the ratio

$$\frac{\Phi_{CO}}{\Phi_{FIR}} = \frac{\Phi_{CO}/\Phi_0}{\Phi_{FIR}/\Phi_0}\,. \tag{8}$$

This ratio is plotted in Figure 13 as a function of $x = h/D$. We can now use the ratio of the measured Y_{CO} to the predicted Y_{CO} to determine the ratio of beam-filling factors

$$\frac{\Phi_{CO}}{\Phi_{FIR}} = \frac{Y_{CO}^{(meas)}}{Y_{CO}^{(pred)}}\,. \tag{9}$$

We have assumed that, except for the geometry/beam-filling factor, the physical parameters remain unchanged as compared to the one-dimensional model. For the 30 Dor northeast peak with a ratio $Y_{CO}^{(meas)}/Y_{CO}^{(pred)} \sim 0.1$ a corresponding value $x = 0.837$ is found (Fig. 13). From that one derives a volume fraction of the CO core $V_{CO}/V_0 = 4\%$ of the clump volume.

Figure 12 can also be used to estimate the beam-filling factor of the PDR by comparing the observed, beam-averaged FUV intensity, χ_{obs}, with the local FUV intensity, χ_{theor} (Wolfire et al. 1989):

$$\Phi_{PDR} = \chi_{obs}/\chi_{theor}\,. \tag{10}$$

For a density range of $n = 10^3$–10^4 cm^{-3} we find a range of UV intensities $\chi_{theor} = 2300$–5100. With an observed UV intensity $\chi_{obs} = 3500$ (Werner et al. 1978), a range of $\Phi_{PDR} = 1.5$–0.69 is found for the beam-filling factor.

For a more accurate estimate we looked for a self-consistent solution by taking a first-order estimate for n from Figure 11*c*) and by then using Figure 12 to get a solution for χ. This process, when iterated, converged rapidly toward a solution with a density of $n = 6800$ cm^{-3} and a UV field of $\chi = 4600$, yielding a beam-filling factor of $\Phi_{PDR} = 0.77$. This beam-filling factor is close enough to unity to justify the use of absolute line intensities for the analysis in §§ 4.4.1 and 4.4.2 instead of line intensity ratios (which would be independent of beam-filling factors).

4.5. *Determination of Clump Size*

For the physical conditions that we find, the PDR models (van Dishoeck & Black 1988; Wolfire, Tielens, & Hollenbach 1990; Sternberg & Dalgarno 1995) predict a C^+ column density of 2×10^{18} cm^{-2} in a solar metallicity environment. If one assumes that the penetration depth of the FUV is controlled by dust extinction and that the dust-to-gas ratio is directly proportional to metallicity, then this column density should be fairly insensitive to changes in metallicity. We therefore adopt this value for the following analysis. For a carbon abundance 1/3.6 solar value, this is equivalent to a hydrogen nuclei column density of 2.4×10^{22} cm^{-2}. The total column density of hydrogen, $N_H + N_{H_2}$, must then be between $N_{tot} = 1.2 \times 10^{22}$ cm^{-2} (all hydrogen in molecular form) and $N_{tot} = 2.4 \times 10^{22}$ cm^{-2} (all hydrogen in atomic form). If the hydrogen molecule is strongly shelf-shielding a major fraction of the hydrogen is expected to be in molecular form (Maloney & Black 1988). Self-shielding, however, will break down if the photodissociation rate is greater than the H_2 formation rate, i.e., when the ratio χ/n exceeds a certain limit. Sternberg (1989) has estimated this limit to be $\chi/n \sim 0.01$ cm^{-3}. With the density and UV field derived in the previous section we find a ratio of $\chi/n = 0.7$ cm^{-3} which indicates that most of the hydrogen in the PDR should actually be in atomic form. Unfortunately, H I observations of the LMC published to date (Luks & Rohlfs 1992; Dickey et al. 1994) do not have enough spatial resolution to distinguish between the two cases. We therefore adopt a value of $N_{tot} \sim 2 \times 10^{22}$ cm^{-2} for the total hydrogen column density. With the simplifying assumption that the clumps all have the same size and the same [C II]–emitting column density N_{tot} and for a beam-filling factor of 1 as estimated above, one can derive their diameter D as

$$D = \frac{N_{tot}}{nx}\,. \tag{11}$$

For $n = 10^4$–10^3 cm^{-3} and $x = 0.84$ we find $D = 0.7$–7 pc. The gas mass contained in each clump is then $M = 70$–$7000\ M_\odot$. For the particular case of $n = 6800$ cm^{-3} the clump diameter is $D = 1$ pc with a mass of $M = 150\ M_\odot$. Clump sizes on that

scale have been directly observed in our Galaxy (Bally et al. 1987; Stutzki & Güsten 1990); our observations show that the ISM in the low-metallicity environment of an irregular galaxy is structured/fragmented in a similar way as in the Galaxy.

It should be pointed out, however, that this number may only be understood as a characteristic size scale; a much more realistic assumption would be a distribution of clump sizes (Stutzki & Güsten 1990). In the smaller clumps the CO would be completely photodissociated, whereas the larger clumps would contribute the observed, beam-averaged CO line intensity.

4.6. *Consequences for the* CO-to-H_2 *Conversion Factor*

The above analysis as well as the use of the ^{12}CO $(1 \rightarrow 0)$ line as a measure of the molecular gas depend on the assumption that the CO $(1 \rightarrow 0)$ line is optically thick. For the clump sizes and corresponding sizes of the CO core, this may no longer be fulfilled and, therefore, needs to be checked. The details of the estimate are given in Appendix B; here we simply quote the results. The optical depth of the CO $(1 \rightarrow 0)$ line, $\tau_{1\rightarrow 0}$, is a function of the temperature, T, which may be substantially higher than in a quiescent molecular cloud. For clump diameters of 0.5–5 pc, one finds optical depths of

$$\tau_{1\rightarrow 0} = \begin{cases} 8\text{–}30 & \text{when } T = 10 \text{ K} \\ 0.5\text{–}2 & \text{when } T = 50 \text{ K} . \end{cases} \quad (12)$$

For cold gas ($T = 10$ K) the CO $(1 \rightarrow 0)$ line will therefore still be optically thick. If the gas is warmer ($T = 50$ K), however, this may no longer be valid, leading actually to a reduced temperature dependence of the observable CO $(1 \rightarrow 0)$ antenna temperature.

Booth & Johansson (1991) and Johansson et al. (1990) have observed both the $(1 \rightarrow 0)$ and $(2 \rightarrow 1)$ lines of ^{12}CO and ^{13}CO toward a few positions in the LMC and derived optical depths $\tau \sim 1$ for the ^{12}CO $(1 \rightarrow 0)$ lines. This modest optical depth and its indication of photodissociation of CO is in good agreement with our conclusions above. Lequeux et al. (1994) report a similar finding for six molecular clouds in the SMC. From their observations of the $(1 \rightarrow 0)$ and $(2 \rightarrow 1)$ transitions of ^{12}CO and ^{13}CO they conclude that the CO emission arises from relatively dense regions ($n \sim 10^4$ cm^{-3}) which they interpret as the denser parts ("clumps") of interstellar clouds whereas the CO in the less dense "interclump" medium is photodissociated.

While the optical depth may not be a major worry, the use of canonical CO-to-H_2 conversion factor critically depends on two quantities, namely, the area filling factor of the CO-emitting gas relative to that of the total, dense, neutral medium, and the ratio of atomic to molecular gas in this medium. Both quantities depend on physical parameters (UV field, density) and morphology (clumpiness, projection angle). In our discussion of geometry effects in § 4.4.3, for example, the reduction of the observed CO core sizes of the spherical clumps would have been much less pronounced for front illumination clumps (along the line of sight) rather than side illumination (perpendicular to the line of sight). Another critical parameter is the self-shielding of the hydrogen molecule. If, depending on density, n, and UV field, χ, self-shielding determines the H/H_2 transition, then this transition will occur much closer to the clump surface than the transition $C^+/C/CO$ (Maloney & Black 1988), and molecular hydrogen will exist through most of the PDR. In this case, there will be a large amount of molecular gas which is not directly traced by CO. This could explain the increased ratio of virial masses to CO $(1 \rightarrow 0)$ integrated line intensities found in the LMC by Cohen et al. (1988). However, for high enough ratios of χ/n, self-shielding can break down, and the H/H_2 transition will be determined by dust extinction of the FUV and approximately coincide with the $C^+/C/CO$ transition. In this case, the CO $(1 \rightarrow 0)$ integrated line intensity would indeed, with the canonical conversion factor, trace the molecular gas. One would, however, still observe the greater virial mass of the whole clump which now would mainly consist of atomic gas. This photodissociated, atomic gas will differ from other phases of the atomic medium (cold neutral medium, warm neutral medium; Kulkarni & Heiles 1987; Heiles 1988) by its higher density which will be similar to that of the molecular gas from which it was formed.

To distinguish between the two cases, a detailed investigation of all phases of the dense, neutral medium is necessary. Observations of [C II] and other PDR tracers are required to determine the amount of gas and the physical conditions in the PDR. If this information allows an unambiguous distinction between H_2 self-shielding versus dust extinction then the CO $(1 \rightarrow 0)$ integrated line intensity should be sufficient to determine the masses of the atomic and the molecular gas; otherwise, the amount of atomic hydrogen in the PDR has to be measured independently, i.e., by an H I 21 cm observation which would at least give an upper limit on the atomic hydrogen in the PDR.

5. CONCLUSIONS

1. We have presented a variety of new observations of the 30 Doradus region: integrated line intensity maps in Brγ, H_2 1–0 $S(1)$, [C II] 158 μm, [O I] 63 μm, and CO $(1 \rightarrow 0)$, and an [O I] 146 μm line spectrum.

2. The source morphology as seen in the Brγ line and in the CO $(1 \rightarrow 0)$ line indicates that the H II region is ionization bounded toward the northeast and southwest molecular peaks but density bounded in the valley between the peaks. The Lyc luminosity derived from the Brγ is somewhat lower than estimated from the census of the exciting stellar cluster; this indicates that part of the UV escapes from the H II region. The ratio of the FUV to the Lyc luminosities matches the average spectral distribution of the exciting stars.

3. The H_2 1–0 $S(1)$ emission appears mixed in with the ionized gas, indicating a highly fragmented structure of the ISM. The observed H_2 line intensity is consistent with thermal emission from dense molecular clumps exposed to the stellar radiation field.

4. From the FIR fine structure lines we deduce densities ($n \approx 6800$ cm^{-3}) and FUV fields ($\chi \approx 4600$) comparable to the conditions in Galactic PDRs.

5. The [C II]/CO $(1 \rightarrow 0)$ line intensity ratio (6×10^4) is about 10 times higher than in Galactic star formation regions; this can only be understood as a geometry effect: in a clumpy medium with low metal abundances, the relative beam-filling factor of the remaining CO cores can be drastically reduced compared to that of the PDR. Modified one-dimensional PDR models can be used to determine this ratio and to deduce a characteristic clump size scale of 1 pc.

6. Most of the molecular mass may be present in PDRs, and a substantial fraction of the molecular gas may be void of CO. Thus, the integrated CO $(1 \rightarrow 0)$ line intensity may not be a reliable tracer of the total molecular component of the ISM. The true H_2/CO conversion factor strongly depends on the

actual physical conditions and morphology and may be up to an order of magnitude higher than the canonical values.

We thank the crew of the Kuiper Airborne Observatory for their constant support, particularly in mastering all kinds of adverse situations "down under." F. Herrmann helped with the observations. We would like to thank R. Genzel and C. H. Townes for stimulating discussions and their interest in this work. M. Rumitz helped with his competent remote advice at odd hours to straighten out FIFI's electronics. This work was supported in part by NASA grant NAG 2-208. N. G. was supported by a Feodor Lynen followship of the Alexander von Humboldt foundation. A. S. thanks the German-Israeli Foundation for Research and Development for support.

APPENDIX A

RADIATIVE TRANSFER CALCULATIONS

For the radiative transfer calculations of the surface brightnesses of the 158 μm [C II] line and of the 63 μm and 146 μm [O I] lines we used the code by Stutzki (1985). The underlying model is a one-dimensional, large velocity gradient (LVG), escape probability approximation. We adopted a velocity span of 20 km s^{-1} for all three lines as suggested by the CO (1–0) line width. The beam-filling factor was assumed to be 1 as could be approximately confirmed in the further analysis (§ 4.4). The radiative transfer code can take into account dust continuum radiation; a correct treatment, however, requires some knowledge about the source morphology, i.e., whether the continuum source is in the background, in the foreground, or mixed in with the line source. Fortunately, the only line in which the continuum level is a substantial fraction of the line emission is the 146 μm [O I] line in which both the dust (Werner et al. 1978) and the line are so optically thin that the morphology is irrelevant. The continuum emission within the line width of the [C II] and the 63 μm [O I] line is small enough to be neglected for the radiative transfer calculations.

For the calculation of the collisional population of the fine-structure levels we used the O^0/He and O^0/H_2 cross sections given by Monteiro & Flower (1987) and Jacquet et al. (1992), and the C^+/H_2 and C^+/H cross sections of Flower & Launay (1977). Our modeling of the three fine-structure lines implicitly assumes that the [C II] and [O I] lines arise from the same volume although the O^0-bearing layer may extend deeper into the molecular gas than the C^+ layer (Herrmann 1994). However, the excitation energy of the [O I] lines is higher than that of the [C II] line, and since in a more realistic model one would assume a temperature drop toward the molecular component, this additional column density of O^0 will not contribute much to the observed [O I] line intensities.

APPENDIX B

OPTICAL DEPTH OF THE CO (1 → 0) LINE

The optical depth $\tau_{1\to0}$ of the CO (1 → 0) line is given by

$$\tau_{1\to0} = \frac{hc^2}{8\pi\nu^2 kT_{\rm ex}} A_{1\to0} \frac{v}{\Delta v} N_1 , \tag{B1}$$

where $A_{1\to0} = 6 \times 10^{-8}$ s^{-1} is the Einstein A-coefficient for the $J = 1 \to 0$ transition and N_1 is the column density of molecules in the $J = 1$ rotational state, given by

$$N_1 = N \times g_1 \exp(-E_1/kT_{\rm ex})/\sum \tag{B2}$$

with the partition function Σ defined as

$$\Sigma = \sum_{j=1}^{\infty} g_j \exp(-E_j/kT_{\rm ex}) . \tag{B3}$$

To get a lower limit for $\tau_{1\to0}$ we assume that the rotational levels are thermalized, i.e., $T_{\rm ex} = T_{\rm kin}$ for all levels. With a relative CO abundance $N_{\rm CO}/N_{\rm H} = 3 \times 10^{-4}/3.6$ for the LMC we get for the optical depth:

$$\tau_{1\to0} = \begin{cases} 8.3 \times 10^{-21} \dfrac{N_{\rm H}^{\rm core}}{\rm cm^{-2}} \Big/ \dfrac{\Delta v}{\rm km\ s^{-1}} & \text{when } T = 10 \text{ K} \\ 5.7 \times 10^{-22} \dfrac{N_{\rm H}^{\rm core}}{\rm cm^{-2}} \Big/ \dfrac{\Delta v}{\rm km\ s^{-1}} & \text{when } T = 50 \text{ K} , \end{cases} \tag{B4}$$

where $N_{\rm H}^{\rm core}$ is the column density of hydrogen nuclei in the CO core and Δv is the line width in km s^{-1} of the CO (1 → 0) emission from one clump. $N_{\rm H}^{\rm core}$ of the core can be estimated to be $(1 - x)N_{\rm H}$ of the whole clump; from the analysis above we adopt a value $N_{\rm H}^{\rm core} \sim 3 \times 10^{21}$ cm^{-2} for the core column density. This translates into an optical depth of

$$\tau_{1\to0} = \begin{cases} 25 \Big/ \dfrac{\Delta v}{\rm km\ s^{-1}} & \text{when } T = 10 \text{ K} \\ 1.7 \Big/ \dfrac{\Delta v}{\rm km\ s^{-1}} & \text{when } T = 50 \text{ K} . \end{cases} \tag{B5}$$

Since the CO ($1 \rightarrow 0$) beam will cover a number of clumps at the same time, the line width of an individual clump can only be estimated. If we assue that each clump is virialized and that the CO core shows the full velocity distribution of the whole clump, then the line width Δv will be given by (Maloney & Black 1988)

$$\Delta v = \sqrt{\Phi \pi G R N_{\rm H} \mu m_{\rm H}}\,, \tag{B6}$$

where Φ is a geometry factor of order unity, G, is the gravitational constant, R is the clump radius, $N_{\rm H} = 2.4 \times 10^{22}$ cm^{-2} is the column density of hydrogen nuclei in the clump, $\mu = 1.1$ is the mass correction factor for the helium in the ISM, and $m_{\rm H}$ is the mass of the hydrogen atom. For clump radii of 0.35–3.5 pc one gets line widths $\Delta v = 0.8$–2.7 km s^{-1}. With these values one gets ranges in optical depth of

$$\tau_{1\rightarrow 0} = \begin{cases} 8\text{–}30 & \text{when } T = 10 \text{ K} \\ 0.5\text{–}0.2 & \text{when } T = 50 \text{ K} \end{cases}. \tag{B7}$$

For cold gas ($T = 10$ K) the CO ($1 \rightarrow 0$) line will therefore still be optically thick. If the gas is warmer ($T = 50$ K), however, this assumption may be no longer valid.

REFERENCES

Bally, J., Langer, W. D., Stark, A. A., & Wilson, R. W. 1987, ApJ, 312, L45
Black, J. H., Porter, A., & Dalgarno, A. 1981, ApJ, 249, 138
Black, J. H., & van Dishoeck, E. F. 1987, ApJ, 322, 412
Bloemen, H. 1989, ARA&A, 154, 25
Booth, R. S., & Johansson, L. E. B. 1991, in IAU Symp. 148, The Magellanic Clouds, ed. R. Haynes & D. Milne (Dordrecht: Kluwer), 157
Boreiko, R. T., & Betz, A. L. 1991, ApJ, 380, L27
Boreiko, R. T., Betz, A. L., & Zmuidzinas, J. 1990, ApJ, 353, 181
Blitz, L. 1987, in Physical Processes in Interstellar Clouds, ed. G. E. Morfill & M. Scholer (Dordrecht: Reidel), 35
Burton, M. G., Hollenbach, D. J., & Tielens, A. G. G. M. 1990, ApJ, 365, 620
Campbell, B., Hunter, D. A., Holtzman, J. A., Lauer, T. R., & Shaya, E. J. 1992, AJ, 104, 1721
Caplan, J., & Deharveng, L. 1985, A&AS, 62, 63
———. 1986, A&A, 155, 297
Clayton, G. C., & Martin, P. G. 1985, ApJ, 288, 558
Cohen, R. S., Dame, T. M., Garay, G., Montani, J., Rubio, M., & Thaddeus, P. 1988, ApJ, 331, 95
Crawford, M. K., Genzel, R., Townes, C. H., & Watson, D. M. 1985, ApJ, 291, 755
Czyzak, S. J., & Aller, L. H. 1977, Ap&SS, 46, 371
De Marchi, G., Nota, A., Leitherer, C., Ragazzoni, R., & Barbieri, C. 1993, ApJ, 419, 658
Dickey, J. M., Mebold, U., Marx, M., Amy, S., Haynes, R. F., & Wilson, W. 1994, A&A, 289, 357
Dickman, R. L., Snell, R., & Schloerb, F. P. 1986, ApJ, 309, 326
Draine, B. T., & Lee, H. M. 1984, ApJ, 285, 89
Draine, B. T., Roberge, W. G., & Dalgarno, A. 1983, ApJ, 264, 485
Draine, B. T., & Woods, D. T. 1990, ApJ, 363, 464
Dufour, R. J. 1984, in IAU Symp. 108, Structure and Evolution of the Magellanic Clouds, ed. S. van den Bergh & K. S. de Boer (Dordrecht: Kluwer), 353
Falgarone, E., & Perault, M. 1988, in Physical Processes in Interstellar Clouds, ed. G. E. Morfill & M. Scholer (Dordrecht: Reidel, 59
Flaud, J.-M., Camy-Peyret, C., & Johns, J. W. C. 1983, Canadian J. Phys., 61, 146
Flower, D. R., & Launay, J. M. 1977, J. Phys. B, 10, 3673
Genzel, R., Hollenbach, D. J., & Townes, C. H. 1994, Rep. Prog. Phys., 57, 417
Genzel, R., Watson, D. M., Crawford, M. K., & Townes, C. H. 1985, ApJ, 297, 766
Goldschmidt, O., & Sternberg, A. 1995, ApJ, 439, 256
Goldsmith, P. 1987, in Interstellar Processes, ed. D. J. Hollenbach & H. A. Thronson (Dordrecht: Reidel), 51
Gredel, R., & Dalgarno, A. 1995, ApJ, 446, 852
Haas, M. R., Hollenbach, D. J., & Erickson, E. F. 1986, ApJ, 301, L57
Heiles, C. 1988, Lecture Notes in Physics, 306, The Outer Galaxy, ed. L. Blitz & F. J. Lockman (Berlin: Springer), 151
———. 1994, ApJ, 436, 720
Herrmann, F. 1994, Ph.D. thesis, Ludwig-Maximilians-Universität München
Hildebrand, R. H., Loewenstein, R. F., Harper, D. A., Orton, G. S., Keene, J., & Whitcomb, S. E. 1985, Icarus, 64, 64
Hollenbach, D. J., & McKee, C. F. 1989, ApJ, 342, 306
Howe, J. E., Jaffe, D. T., Genzel, R., & Stacey, G. J. 1991, ApJ, 373, 158
Israel, F. P. 1988, in Millimeter and Submillimeter Astronomy, ed. R. D. Wolstencroft & W. B. Burton (Dordrecht: Kluwer), 281
Jaffe, D. T., Davidson, J. A., Dragovan, M., & Hildebrand, R. H. 1984, ApJ, 284, 637
Jaquet, R., Staemmler, V., Smith, M. D., & Flower, D. R. 1992, J. Phys. B, 25, 285
Johansson, L. E. B., Booth, R. S., Murphy, D. M., & Olberg, M. 1990, in Submillimetre Astronomy, ed. G. D. Watts & A. S. Webster (Dordrecht: Kluwer), 287
Kennicutt, R. C. 1984, ApJ, 287, 116
Koornneef, J. 1982, A&A, 107, 247
Krabbe, A., et al. 1993, PASP, 105, 1472
Kulkarni, S., & Heiles, C. 1987, in Interstellar Processes, ed. D. J. Hollenbach & H. A. Thronson (Dordrecht: Reidel), 87
Lequeux, J., Le Bourlot, J., Pineau des Fôrets, G., Roueff, E., Boulanger, F., & Rubio, M. 1994, A&A, 292, 371
Luks, T., & Rohlfs, K. 1992, A&A, 263, 41
Madden, S. C., Geis, N., Genzel, R., Herrmann, F., Jackson, J. M., Poglitsch, A., Stacey, G. J., & Townes, C. H. 1993, ApJ, 407, 579
Madden, S. C., et al. 1995, in preparation
Maloney, P., & Black, J. H. 1988, ApJ, 325, 389
Meixner, M., Haas, M. R., Tielens, A. G. G. M., Erickson, E. F., & Werner, M. 1992, ApJ, 390, 499
Mochizuki, K., et al. 1994, ApJ, 430, L37
Monteiro, T. S., & Flower, D. R. 1987, MNRAS, 228, 101
Morgan, D. H., & Nandy, K. 1982, MNRAS, 199, 979
Osterbrock, D. E. 1989, Astrophysics of Gaseous Nebulae and Active Galactic Nuclei (Mill Valley: University Science Books)
Panagia, N. 1973, AJ, 78, 929
Poglitsch, A., et al. 1991, Int. J. Infrared Millimeter Waves, 12, 895
Poglitsch, A., Geis, N., Genzel, R., Herrmann, F., Madden, S. C., Stacey, G. J., & Townes, C. H. 1992, in The Evolution of Galaxies and Their Environment, Proc. Third Teton Summer School on Astrophysics, ed. D. Hollenbach, H. Thronson, & J. M. Shull (Moffett Field: NASA), 187
Rotaciuc, V., Krabbe, A., Cameron, M., Drapatz, S., Genzel, R., Sternberg, A., & Storey, J. W. V. 1991, ApJ, 370, L23
Sanders, D. B., Scoville, N. Z., & Solomon, P. M. 1985, ApJ, 289, 373
Savage, B. D., & Mathis, J. S. 1979, ARA&A, 17, 73
Stacey, G. J., Beeman, J. W., Haller, E. E., Geis, N., Poglitsch, A., & Rumitz, M. 1992, Int. J. Infrared Millimeter Waves, 13, 1689
Stacey, G. J., Geis, N., Genzel, R., Lugten, J. B., Poglitsch, A., Sternberg, A., & Townes, C. H. 1991a, ApJ, 373, 423
Stacey, G. J., Townes, C. H., Poglitsch, A., Madden, S. C., Jackson, J., Hermann, F., Genzel, R., & Geiss, N. 1991b, ApJ, 382, L37
Sternberg, A. 1988, ApJ, 332, 400
———. 1989, ApJ, 347, 863
———. 1993, in The Nearest Active Galaxies, ed. J. Beckman, L. Colina, & H. Netzer (Madrid: Consejo Superior de Investigaciones Científicas), 33
Sternberg, A., & Dalgarno, A. 1989, ApJ, 338, 197
———. 1995, ApJS, 99, 565
Strong, A. W., et al. 1988, A&A, 207, 1
Stutzki, J. 1985, Ph.D. thesis, Universität Köln
Stutzki, J., & Güsten, R. 1990, ApJ, 356, 513
Stutzki, J., Stacey, G. J., Genzel, R., Harris, A. I., Jaffe, D. T., & Lugten, J. B. 1988, ApJ, 332, 379
Tielens, A. G. G. M., & Hollenbach, D. 1985a, ApJ, 291, 722
———. 1985b, ApJ, 291, 747
van Dishoeck, E. F., & Black, J. H. 1988, ApJ, 334, 771
Walborn, N. R. 1991, in IAU Symp. 148, The Magellanic Clouds, ed. R. Haynes & D. Milne (Dordrecht: Kluwer), 145
Werner, M. W., Becklin, E. E., Gatley, I., Ellis, M. J., Hyland, A. R., Robinson, G., & Thomas, J. A. 1978, MNRAS, 184, 365
Westerlund, B. E. 1990, Astron. Astrophys. Rev., 2, 29
Wolfire, M., Hollenbach, D., & Tielens, A. G. G. M. 1989, ApJ, 344, 770
———. 1993, ApJ, 402, 195
Wolfire, M. G., Tielens, A. G. G. M., & Hollenbach, D. 1990, ApJ, 358, 116
Wright, E. L., & Odenwald, S. 1980, BAAS, 12, 456
Ye, T., Turtle, A. J., & Kennicutt, R. C. 1991, in Stars and Active Galaxies, ed. Q. Li (Singapore: World Scientific), 146
Young, J. S., & Scoville, N. Z. 1982, ApJ, 258, 467
Zhou, S., Jaffe, D. T., Howe, J. E., Geis, N., Herrmann, F., Madden, S. C., Poglitsch, A., & Stacey, G. J. 1993, ApJ, 419, 190